HHS Public Access

Author manuscript

Cell Rep. Author manuscript; available in PMC 2025 March 20.

Published in final edited form as:

Cell Rep. 2025 February 25; 44(2): 115231. doi:10.1016/j.celrep.2025.115231.

The Hao-Fountain syndrome protein USP7 regulates neuronal connectivity in the brain via a novel p53-independent ubiquitin signaling pathway

Hao Chen[1,2], **Cole J. Ferguson**[2,3], **Dylan C. Mitchell**[4], **Isabel Risch**[5], **Amanda Titus**[6], **Joao A. Paulo**[4], **Andrew Hwang**[1], **Loren K. Beck**[1], **Tsen-Hsuan Lin**[7], **Wei Gu**[8], **Sheng-Kwei Song**[7], **Carla M. Yuede**[6], **Hiroko Yano**[1,9,10], **Obi L. Griffith**[5], **Malachi Griffith**[5], **Steven P. Gygi**[4], **Azad Bonni**[2,11,*], **Albert H. Kim**[1,9,10,12,13,*]

[1]Department of Neurological Surgery, Washington University School of Medicine, St. Louis, MO 63110, USA

[2]Department of Neuroscience, Washington University School of Medicine, St. Louis, MO 63110, USA

[3]Department of Pathology, University of California, San Diego, La Jolla, CA 92093, USA

[4]Department of Cell Biology, Harvard Medical School, Boston, MA 02115, USA

[5]Department of Medicine, Washington University School of Medicine, St. Louis, MO 63130, USA

[6]Department of Psychiatry, Washington University School of Medicine, St. Louis, MO 63130, USA

[7]Department of Radiology, Washington University School of Medicine, St. Louis, MO 63110, USA

[8]Institute for Cancer Genetics, Department of Pathology and Cell Biology, Columbia University, New York, NY 10032, USA

[9]Department of Neurology, Washington University School of Medicine, St. Louis, MO 63110, USA

[10]Department of Genetics, Washington University School of Medicine, St. Louis, MO 63110, USA

[11]Roche Pharma Research and Early Development, Neuroscience and Rare Disease Discovery and Translational Area, Roche Innovation Center, 4070 Basel, Switzerland

[12]The Brain Tumor Center, Siteman Cancer Center, Washington University School of Medicine, St. Louis, MO 63110, USA

[*]Correspondence: bonni@wustl.edu (A.B.), alberthkim@wustl.edu (A.H.K.).

AUTHOR CONTRIBUTIONS

Conceptualization, H.C., C.J.F., A.H.K., and A.B.; investigation, H.C., D.C.M., A.T., J.A.P., L.B., and T.-H.L.; formal analysis, H.C., D.C.M., I.R., J.A.P., A.H., T.-H.L., and C.M.Y.; resources, W.G.; supervision, H.Y., S.-K.S., C.M.Y., O.L.G., M.G., S.P.G., A.B., and A.H.K.; validation, H.C. and A.H.; visualization, H.C. and C.J.F.; funding acquisition, H.Y., J.A.P., S.P.G., A.B., and A.H.K.; writing – original draft, H.C.; writing – review & editing, C.J.F., H.Y., A.B., and A.H.K.

DECLARATION OF INTERESTS

A.H.K. is a consultant for Monteris Medical and has received a research grant from Stryker to study a dural substitute, both of which have no direct relation to this study. A.B. is a full-time employee and shareholder of F. Hoffmann-La Roche Ltd.

SUPPLEMENTAL INFORMATION

Supplemental information can be found online at https://doi.org/10.1016/j.celrep.2025.115231.

[13]Lead contact

SUMMARY

Mutation or deletion of the deubiquitinase USP7 causes Hao-Fountain syndrome (HAFOUS), which is characterized by speech delay, intellectual disability, and aggressive behavior and highlights important unknown roles of USP7 in the nervous system. Here, we conditionally delete USP7 in glutamatergic neurons in the mouse forebrain, triggering disease-relevant phenotypes, including sensorimotor deficits, impaired cognition, and aggressive behavior. Although USP7 deletion induces p53-dependent neuronal apoptosis, most behavioral abnormalities in USP7 conditional knockout mice persist following p53 loss. Strikingly, USP7 deletion perturbs the synaptic proteome and dendritic spinogenesis independent of p53. Integrated proteomics and biochemical analyses identify the RNA splicing factor Ppil4 as a key substrate of USP7. Ppil4 knockdown phenocopies the effect of USP7 loss on dendritic spines. Accordingly, USP7 loss disrupts splicing of synaptic genes. These findings reveal that USP7-Ppil4 signaling regulates neuronal connectivity in the developing brain with implications for our understanding of HAFOUS pathogenesis and other neurodevelopmental disorders.

In brief

Chen et al. demonstrate that the Hao-Fountain syndrome protein, the deubiquitinase USP7, regulates disease-relevant behaviors and synapse development via p53-independent pathways. Further, extensive proteomics, biochemical, and splicing analyses reveal that USP7 interacts with and deubiquitinates the RNA splicing factor Ppil4 to regulate the molecular composition and morphogenesis of the synapse.

Graphical abstract

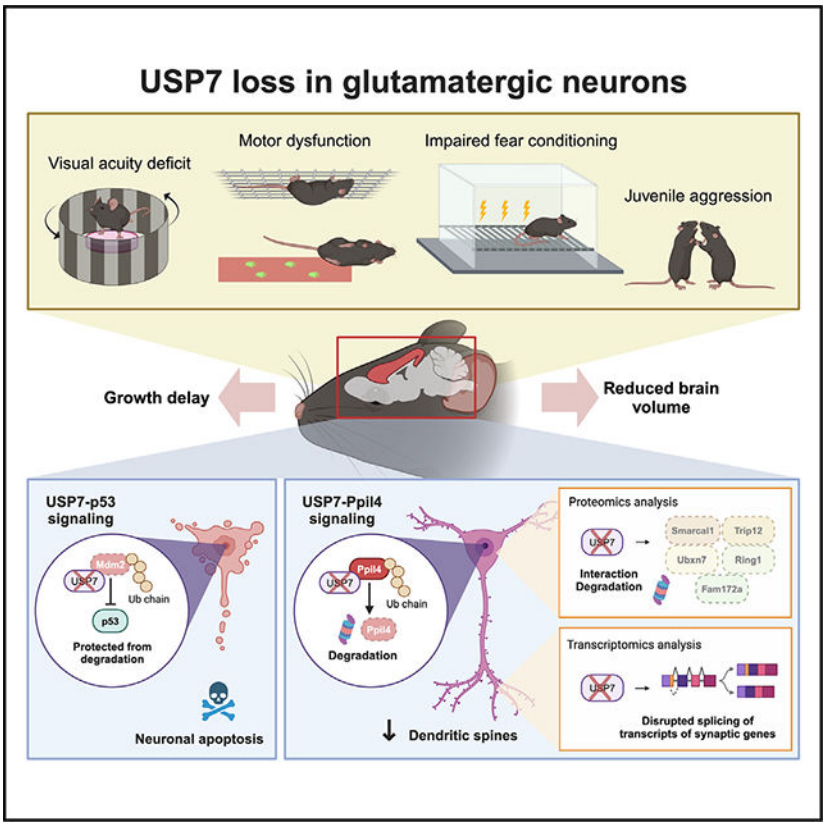

INTRODUCTION

As a fundamental post-translational modification, protein ubiquitination plays critical roles in neuronal development and function, and deregulation of ubiquitination is thought to contribute to the pathogenesis of diverse neurological conditions, including Angelman,[1] Gordon-Holmes,[2,3] and Ferguson-Bonni[4] syndromes. Ubiquitination is regulated by both ubiquitin ligases, which catalyze the covalent attachment of ubiquitin to specific substrates, and deubiquitinases, which catalyze the removal of ubiquitin from specific substrates. Although ubiquitin ligases have been studied extensively in neurodevelopment,[5] the functions of most deubiquitinases in the nervous system have remained largely unexplored[6] despite their link with neurodevelopmental disorders in genetic association studies.[7] Here, we characterized the role of the deubiquitinase ubiquitin-specific protease 7 (USP7) in the mammalian brain. Deletion or mutation of *USP7* causes Hao-Fountain syndrome (HAFOUS), which is characterized by developmental delay, intellectual disability, and aggressive behavior.[8,9] However, the neuropathogenesis of HAFOUS has remained poorly understood.

Studies in cancer biology have revealed that USP7 induces turnover of the tumor suppressor protein p53,[10,11] and, thus, inhibition of USP7 may hold therapeutic promise for suppressing tumor growth.[12,13] A key target of USP7 is the ubiquitin ligase Mdm2, which ubiquitinates p53 and thereby promotes p53 degradation. USP7 counteracts the effects of Mdm2 auto-ubiquitination to stabilize Mdm2 and promote Mdm2-dependent ubiquitination and

consequent degradation of p53.[11] In mice, global loss of *Usp7* leads to early embryonic lethality, indicating that USP7 is essential for embryogenesis.[14] Deletion of USP7 in neural stem cells leads to reduced brain size, perinatal lethality, and p53 accumulation.[15] Although loss of *Trp53*, the gene encoding p53 in mice, rescues brain size in *Usp7* mutant mice, co-deletion of p53 fails to improve newborn survival, suggesting that USP7 plays essential roles in the nervous system through unknown p53-independent mechanisms.[15] Importantly, whereas USP7 function in proliferating cells has been the subject of intense scrutiny,[16–18] the roles and mechanisms of USP7 in post-mitotic neurons that might be relevant to the pathogenesis of HAFOUS are largely unknown.

RESULTS

Conditional deletion of USP7 in glutamatergic neurons alters mouse behavior

To characterize the role of USP7 in post-mitotic glutamatergic neurons of the forebrain, we crossed mice harboring floxed *Usp7* alleles ($Usp7^{fl/fl}$) with mice expressing the recombinase Cre under the control of the regulatory sequence of the *NEX* gene (*NEX-cre*).[19] Immunofluorescence analyses of the embryonic cortex of $Usp7^{fl/fl}$; *NEX-cre* (hereafter called *Usp7* cKO) mice demonstrated that USP7 is depleted in neurons of the cortical plate but not in the ventricular zone, confirming that USP7 is deleted specifically in post-mitotic neurons (Figure 1A). Further analyses of the young adult cortex showed that loss of USP7 was restricted in NeuN-positive cortical neurons of *Usp7* cKO mice (Figure 1B).

Patients with HAFOUS exhibit a range of deficits early in life, including growth retardation, hypotonia, visual impairment, gait abnormalities, aggression, and autism with intellectual disability[9] (Figure 1L). To ascertain the effects of USP7 deletion at the organismal level, we subjected *Usp7* cKO, *Usp7* cHet ($Usp7^{fl/+}$; *NEX-cre*), and *Usp7* WT ($Usp7^{fl/fl}$) mice to a battery of behavioral tests and biometric measurements (Figures 1C–1K and S1). Although *Usp7* cKO mice exhibited a small size during the juvenile period, the body weight of adult *Usp7* cKO mice was similar to that of controls (Figures S1A–S1C).

Visual deficits are common in HAFOUS.[9] To examine visual function in *Usp7* cKO mice, we employed the virtual optomotor system (VOS). In this experiment, mice make reflexive head movements to track the rotation of alternating black and white vertical stripes, the spatial frequency of which can be varied experimentally. We found that *Usp7* cKO mice stopped responding at a much lower spatial frequency, suggesting reduced visual acuity (Figure 1C).

Hypotonia is a motor impairment associated with HAFOUS.[8,9] To assess motor performance in *Usp7* cKO mice, we began with the inverted screen test. In this strength test, *Usp7* cKO mice exhibited a significant reduction in the latency to fall (Figure 1D). We next evaluated motor coordination using the ledge, platform, and pole tests. *Usp7* cKO mice displayed reduced time of maintaining balance before falling or slipping off the ledge and platform (Figures S1D and S1E) and were slower to turn around on the pole (Figure S1G). However, mice of all genotypes spent similar amounts of time climbing down the pole

(Figure S1F). These results indicate that USP7 loss in the forebrain impairs motor strength and coordination without affecting simple motor tasks.

Another motor deficit in HAFOUS is abnormal gait.[9] Noticeably, *Usp7* cKO mice exhibited abnormal splaying of the hindlimbs during voluntary locomotion (Video S1). We then employed the CatWalk XT system to systematically analyze mouse gait (Video S2) and found that *Usp7* cKO mice placed extra weight onto their hindpaws (Figure 1E) and exhibited an increase in the swing speed of the limbs (Figures 1F, S1H, and S1I).

We next evaluated *Usp7* cKO mice in tests of learning and memory. To avoid the potentially confounding effect of visual impairment, we chose fear conditioning with an auditory cue. Using an acoustic startle test, we confirmed that hearing was not impaired in *Usp7* cKO mice (Figure S1J). On day 1, mice were exposed to an auditory tone (cue) in a peppermint-scented chamber (context) prior to the delivery of a mild electrical shock to the paw (Figure 1G). On day 2, during re-exposure to the context environment, *Usp7* cKO mice exhibited reduced freezing behavior (conditioned response) (Figure 1H), suggesting diminished association between the context (conditioned stimulus) and the shock (unconditioned stimulus). On day 3, upon re-exposure to the auditory cue (conditioned stimulus) in a distinct context environment, *Usp7* cKO mice also exhibited diminished freezing behavior (Figure 1I). In contrast, despite visual impairment, *Usp7* cKO mice showed no deficits in the Y maze test of spatial working memory (Figure S1K). These results demonstrate that USP7 depletion in glutamatergic neurons causes specific deficits in associative learning.

Strikingly, *Usp7* cKO mice displayed aggressive behavior in the form of violent attacks on cagemates that resulted in wounds and, occasionally, amputation of the other animal's tail (Video S3). Between the ages of 3 and 12 weeks, 9 of 29 *Usp7* cKO mice inflicted bite marks centered around the tails of co-caged mice (Figure 1J). We observed the tail-biting behavior in both sexes of *Usp7* cKO mice but with a higher percentage among male mice (42.86%) than female mice (20.00%) (Figure 1K). This tail-biting behavior is highly unusual and distinct from the commonly observed biting associated with social aggression, which occurs after sexual maturity and typically targets the lower back and abdomen.[20]

In summary, these behavioral analyses demonstrate that USP7 loss in glutamatergic neurons of the forebrain causes a suite of deficits that mimic the clinical hallmarks of HAFOUS, including the unusual phenotype of aggression[8,9] (Figure 1L). These results suggest that USP7 may play conserved roles in the brains in humans and mice. Therefore, investigation of *Usp7* cKO mice may provide valuable insights into ubiquitin signaling during brain development and the pathogenesis of HAFOUS.

USP7 prevents p53-dependent neuronal apoptosis

After characterizing the diverse behavioral effects of USP7 conditional knockout, we sought to determine how USP7 regulates neuronal development in the cerebral cortex. Therefore, we performed histological analyses at different stages of neurodevelopment, beginning on embryonic day 12 (E12) to coincide with the onset of *NEX-cre* expression.[19] The earliest phenotype we detected was a marked increase in the number of cells positive for the

apoptosis marker protein cleaved caspase-3 (c-cas-3) by immunofluorescence in the cerebral cortex in *Usp7* cKO mice (Figure 2A). Importantly, this phenotype in *Usp7* cKO mice was temporally restricted to the post-natal day 0 (P0) time point, as little signal of c-cas-3 was present at E15, P5, or P10. We next asked whether the apoptosis in the cerebral cortex of *Usp7* cKO mice is cell autonomous. First, co-immunofluorescence analyses demonstrated considerable overlap between Cre and c-cas-3 (Figure S2A), suggesting that apoptosis occurs in Cre-expressing glutamatergic neurons. Second, RNAi-induced knockdown of USP7 in mouse primary cortical neurons using sparse transfection robustly induced apoptosis (Figures S2B–S2D). Together, these results suggest that USP7 loss triggers a perinatal wave of apoptosis in the cerebral cortex in a cell-autonomous manner.

Because USP7 regulates the Mdm2-p53 pathway in cancer and proliferating cells[9,10,14] (Figure 2B), we asked whether the apoptosis in post-mitotic neurons upon USP7 knockout in the mouse cerebral cortex is mediated by p53. We crossed the *Usp7* cKO mice with mice harboring a null allele in *Trp53*, the gene that encodes p53 in mice. Notably, the loss of just one *Trp53* allele in *Usp7* cKO mice reduced the c-cas-3 signal on P0 to a level comparable to controls (Figures 2C and 2D). Homozygous knockout of *Trp53* conferred minimal additional rescue in apoptosis compared to heterozygous deletion of p53 (Figure S2E). To test whether the rescue of apoptosis in *Usp7* cKO neurons by p53 loss is cell autonomous, we employed primary cortical neurons dissociated from E15 mouse embryos harboring floxed *Usp7* (*Usp7*$^{fl/fl}$) and different *Trp53* genotypes. Following transduction with lentiviruses encoding Cre, immunocytochemical analyses confirmed loss of USP7 upon Cre transduction (Figure S2F). As a negative control, neurons transduced with a catalytically dead Cre-Y331F mutant (Cre dead) failed to show depletion of USP7. In cortical neurons dissociated from *Usp7*$^{fl/fl}$; *Trp53*$^{+/+}$ embryos, loss of USP7 following wild-type Cre (Cre WT) transduction substantially reduced cell viability in the MTS assay, whereas neurons from *Usp7*$^{fl/fl}$; *Trp53*$^{+/-}$ and *Usp7*$^{fl/fl}$; *Trp53*$^{-/-}$ embryos demonstrated no significant decrease in viability upon Cre expression (Figure S2G). These results suggest that p53 mediates USP7 deletion-induced apoptosis in a cell-autonomous manner.

The finding of neuronal apoptosis also led us to ask whether this cellular phenotype might translate to a reduction in brain volume. Using diffusion-weighted *ex vivo* MRI, we found that the volumes of both the cerebral cortex and the hippocampus were reduced dramatically by ~40% in *Usp7* cKO mice (Figures S2H and S2I; Table S1). Surprisingly, although p53 loss rescued apoptosis in the brains of *Usp7* cKO mice, co-deletion of p53 in *Usp7* cKO mice had a minimal effect on the volumes of the cerebral cortex or hippocampus (Table S1; Figures S2H and S2I). In agreement with these observations in the forebrain, total brain volume was reduced by ~20% in *Usp7* cKO mice regardless of p53 deletion (Figure S2I; Table S1). These results suggest that p53-mediated apoptosis is not the major contributor to brain volume reduction in *Usp7* cKO mice, indicating the importance of p53-independent pathways.

p53 reduction rescues only a subset of behavioral abnormalities in *Usp7* cKO mice

To determine whether dysregulation of p53 contributes to organism-level deficits in *Usp7* cKO mice, we measured body weight and tested motor performance and memory formation

in mice of the genotype *Usp7*$^{fl/fl}$; *NEX-cre*; *Trp53*$^{+/-}$ (*Usp7* cKO; *Trp53*$^{+/-}$) (Figures 2E–2M and S3A–S3I). The growth of *Usp7* cKO; *Trp53*$^{+/-}$ juvenile mice remained delayed compared to control mice of the genotypes *Usp7*$^{fl/fl}$; *Trp53*$^{+/-}$ (*Usp7* WT; *Trp53*$^{+/-}$) and *Usp7*$^{fl/+}$; *NEX-cre*; *Trp53*$^{+/-}$ (*Usp7* cHet; *Trp53*$^{+/-}$) (Figures S3A and S3B). In contrast, *Usp7* cKO; *Trp53*$^{+/-}$ mice demonstrated visual acuity comparable to *Usp7* WT; *Trp53*$^{+/-}$ mice (Figure 2E). To exclude the possibility that p53 deletion alone impacts visual acuity, which might contribute to the observed difference between *Usp7* cKO and *Usp7* cKO; *Trp53*$^{+/-}$ mice, we also subjected a separate cohort of *Trp53*$^{+/-}$ and *Trp53*$^{+/+}$ mice to the VOS test but failed to observe any deficit (Figure S3C).

Assessment of motor function in *Usp7* cKO; *Trp53*$^{+/-}$ mice demonstrated persistent impairment in the inverted screen test (Figure 2F). Similarly, *Usp7* cKO; *Trp53*$^{+/-}$ mice were also impaired in the ledge, platform, and pole tests (Figures S3D–S3G). p53 co-deletion also failed to normalize the performance of *Usp7* cKO mice in the CatWalk, as *Usp7* cKO; *Trp53*$^{+/-}$ mice also showed improperly distributed body weight and increased swing speed of the limbs (Figures 2G and 2H, S3H, and S3I; Video S4). Tail-biting behavior was also present in *Usp7* cKO; *Trp53*$^{+/-}$ mice (Figures 2L and 2M).

Finally, we analyzed the effect of p53 loss on the impaired associative learning of *Usp7* cKO mice. Similar to *Usp7* cKO mice, *Usp7* cKO; *Trp53*$^{+/-}$ mice exhibited normal hearing in the acoustic startle test (Figure S3J) and reduced freezing during contextual conditioning (Figures 2I and 2J). During cued conditioning, the attenuated freezing response to the auditory cue in *Usp7* cKO mice was corrected in *Usp7* cKO; *Trp53*$^{+/-}$ mice (Figure 2K). Again, we tested *Trp53*$^{+/-}$ and *Trp53*$^{+/+}$ mice in the same auditory cued conditioning and found no effect of p53 deletion itself (Figures S3K–S3M). During contextual conditioning, however, *Trp53*$^{+/-}$ mice exhibited slightly less freezing than *Trp53*$^{+/+}$ mice (Figure 3L), consistent with our observation that *Usp7* WT; *Trp53*$^{+/-}$ mice displayed slightly less freezing at baseline than *Usp7* WT mice despite persistent deficits upon USP7 loss (Figures 1H and 2J). Altogether, these behavioral analyses demonstrate that p53 contributes to USP7 loss-induced impairment of vision and cued fear conditioning, but most behavioral deficits in *Usp7* cKO mice are independent of p53 and its effects on apoptosis (Table S1).

USP7 regulates synapses in the cerebral cortex

The finding that most phenotypes upon USP7 loss were independent of p53 motivated us to identify additional USP7-dependent neuronal phenotypes beyond p53-mediated apoptosis. To probe molecular abnormalities arising from depletion of USP7 in the developing brain, we profiled the proteome of the cerebral cortex of *Usp7* cKO mice using tandem mass tag-mass spectrometry (TMT-MS) (Figure 3A). We included cortices from 5 pairs of sex-matched *Usp7* cKO mice and control littermates at age P17 (principal-component analysis in Figure S4A). We then sorted the differentially abundant proteins based on fold change and adjusted *p* value (Figure 3B). Gene set enrichment analysis (GSEA) showed that the most significantly enriched gene sets were among the down-regulated proteins and consisted predominantly of synapse-related gene sets (Figure 3C). Additional Gene Ontology (GO) overrepresentation analysis using the GOrilla algorithm[21] also identified synapse-related terms among the ranked list of proteins down-regulated upon USP7 loss

(Figure 3D). Further SynGO analysis[22] revealed that both postsynapse and presynapse terms were enriched in these downregulated proteins (Figures S4B–S4D). In contrast, although more proteins were upregulated than downregulated in the cerebral cortex of *Usp7* cKO mice (Figure 3B), no GO terms were significantly overrepresented in these upregulated proteins, whereas GSEA revealed weak enrichment in the chromatin-modifying Spt-Ada-Gcn5 acetyltransferase (SAGA) complex, histone deubiquitination, and the spliceosome among the upregulated proteins (Figure S4E). Overall, these results suggest that USP7 regulates synaptic proteins in the cerebral cortex.

To determine whether USP7 loss impairs synapse development, we next examined dendritic spines of glutamatergic neurons upon USP7 loss *in vivo*. To visualize dendritic spines, we employed the adeno-associated virus (AAV) PHP.eB harboring a Syn-GFP-P2A-GFPf construct to drive expression of cytoplasmic GFP and membrane-bound GFPf in neurons. The AAV was injected into the ventricles of newborn *Usp7* WT and *Usp7* cKO mouse pups at titers that produced sparse labeling of neurons to highlight dendritic spine morphology (Figure 3E). To avoid the influence of p53-mediated apoptosis in neurons, we analyzed the morphologic effects of USP7 loss on the $Trp53^{+/-}$ background. Spine density within both apical and basal dendrites of pyramidal neurons in the motor cortex of *Usp7* cKO; $Trp53^{+/-}$ mice at P18 was significantly reduced compared to that of *Usp7* WT; $Trp53^{+/-}$ mice (Figures 3F–3I). Spine shape analyses showed increased filopodial spines in *Usp7* cKO; $Trp53^{+/-}$ neurons (Figures S4F–S4L). For assessment of dendrite morphology, we returned to Cre-transduced $Usp7^{fl/fl}$; $Trp53^{+/-}$ primary cortical neurons and found no change in dendritic length or arborization upon USP7 loss (Figures S4M–S4S). These results demonstrate that USP7 loss specifically perturbs dendritic spines of cortical pyramidal neurons.

Defining the interactome of the USP7 TRAF domain in cortical neurons

Having identified p53-independent roles of USP7 in dendritic spines, we next examined the mechanism by which USP7 controls synapse formation in post-mitotic neurons. Because substrates of USP7 in cancer cells frequently bind to the TRAF (tumor necrosis factor receptor-associated factor) domain of USP7[18,23] (Figure 4A), we sought to identify neuronal substrates of USP7 among interactors of the TRAF domain in rat primary cortical neurons. Co-immunoprecipitation (coIP) analyses confirmed that the truncated USP7 TRAF domain interacts with the known USP7 substrate Mdm2. Alanine substitutions at key residues of the TRAF domain, including Arg104, Asp165, and Trp166, collectively termed the RDW mutations, disrupted the interaction between the TRAF domain and Mdm2 (Figure S5A). Immunocytochemical analyses in primary cortical neurons confirmed the nuclear localization of both wild-type (WT) and RDW mutant TRAF domains (Figures S5B and S5C). Silver staining of lysates from primary cortical neurons expressing lentiviral FLAG-tagged TRAF domain showed many proteins that co-immunoprecipitated with the WT TRAF domain. Most of these putative interactions were lost with the RDW mutations (Figure 4B). Using the RDW mutant as a negative control, we performed MS analysis of interactors of the USP7 TRAF domain (IP-MS) in 3 biological replicates of primary cortical neurons (principal-component analysis in Figure S5D). We ranked the interactors with the WT TRAF domain in neurons according to protein length-normalized spectral counts and generated an association network of the top 50 interactors based on the STRING (Search

Tool for the Retrieval of Interacting Genes/Proteins) database.[24] GO terms of cellular components revealed a few densely interconnected structures, including ribonucleoprotein complexes, the spliceosome, and the SWI/SNF (BAF) chromatin remodeling complex (Figures 4C and 4D). These results indicate that USP7 interacts with and/or target substrates involved in chromatin and RNA regulation.

Among our interactors of the USP7 TRAF domain, several were associated with neurodevelopmental diseases (e.g., Ddx3x, Nbea, Smarcc2, and Map1b). Therefore, we performed hypergeometric tests with curated neurodevelopmental disease gene sets[25] and found that the USP7 TRAF interactors were most significantly enriched in the gene sets for intellectual disability and autism (Figure 4E), which are also the most common comorbidities in HAFOUS.[9] These USP7 TRAF interactors also had strong enrichment in the high-confidence mRNA targets of the fragile X syndrome protein FMRP[26] (Figure 4E). These observations suggest that USP7 interacts with proteins implicated in neurodevelopmental disorders.

Acute loss of USP7 transforms the proteome of cortical neurons

Because USP7 stabilizes its substrates by removing ubiquitin and preventing subsequent degradation, we also searched for candidate USP7 substrates by profiling protein abundance using quantitative TMT-MS (Figure 5A). To minimize secondary effects following extended loss of USP7, such as those in *Usp7* cKO brain, we acutely depleted USP7 by transducing Cre-expressing lentiviruses into primary cortical neurons of $Usp7^{fl/fl}$; $Trp53^{-/-}$ mouse embryos. Immunoblot analyses confirmed progressive depletion of USP7 in primary neurons expressing WT Cre but not dead Cre (Figure 5B). Based upon the timing of USP7 depletion, we selected day in vitro 6 (DIV6) and DIV8 for TMT proteomics analysis. Consistent with the immunoblot analyses, the TMT abundance of USP7 protein decreased at both DIV6 and DIV8 in neurons expressing WT Cre (Figure 5D). In the principal-component analysis (Figure S6A), the first principal component separated samples at DIV6 from samples at DIV8, whereas the second principal component separated WT versus dead Cre samples. Interestingly, the distance between WT Cre versus dead Cre samples increased from DIV6 to DIV8, consistent with more complete depletion of USP7 on DIV8. These results demonstrate that acute USP7 loss induces a progressive remodeling of the proteome of primary cortical neurons.

Since USP7 stabilizes its substrates, we reasoned that the abundance of USP7 and its substrates should be correlated across all samples. Therefore, we sorted out candidate substrates of USP7 using two metrics: the Euclidian distance between USP7 and each detected protein, which quantitates how similar the TMT abundance profile of each protein is to that of USP7, and the adjusted p value of Cre-dependent effects for each protein using two-way ANOVA (Figure 5C). The TMT abundance of each candidate substrate was downregulated by expression of WT Cre on both DIV6 and DIV8 (Figure 5D). As proof of principle, this approach identified the known USP7 substrate Trim27.[8] Among the other candidate substrates of USP7 were the SWI/SNF chromatin remodeler Smarcal1, the RNA spliceosome proteins Ppil4 and Fam172a, and several ubiquitin ligases, including Trip12 and Ring1 (Figures 5C and 5D). We next confirmed that these candidate substrates identified

in primary cortical neurons also decreased in the cerebral cortex of *Usp7* cKO mice in our previous *in vivo* TMT-MS analysis (Figure S6B). Further immunoblot analysis of the P0 cerebral cortex of *Usp7* cKO; *Trp53*$^{+/-}$ mice showed marked depletion of several candidate substrates, including Ppil4, Ubxn7, Sub1, Smarcal1, Ring1, Fam172a, and Trip12 (Figures 5E and 5F). In contrast, RT-qPCR analysis showed no effect on any of the corresponding RNAs upon USP7 loss (Figure 5G), suggesting that USP7 regulates the abundances of these candidate substrates at the protein level. Altogether, these results demonstrate that USP7 regulates the abundance of specific candidate substrates in primary neurons and in the brain.

To gain insight into the molecular network regulated by USP7, we used weighted correlation network analysis (WGCNA) to cluster proteins that become differentially abundant upon USP7 loss. WGCNA identified 10 distinct modules (Figure S6C). The yellow module, which contained most of the candidate substrates, showed downregulation of its eigengene upon USP7 loss (Figures S6D and S6E). GO analysis of proteins in the yellow module revealed an enrichment in ubiquitin transferase (Figure S6F). Interestingly, ribonucleoprotein and splicing-related GO terms were overrepresented in the turquoise module, which consisted of the largest set of differentially abundant proteins among all modules (Figures S6C and S6F). These unbiased analyses collectively demonstrate that USP7 regulates a diverse network of neuronal proteins.

USP7 targets Ppil4 to regulate synapse development

After profiling the interactome and putative targets of USP7 in neurons, we leveraged these datasets to identify biologically relevant USP7 targets in neurons. TMT proteomics followed by immunoblot validation *in vivo* revealed that USP7 stabilizes Ppil4, Ubxn7, Sub1, Smarcal1, Ring1, Fam172a, and Trip12. Because reduced dendritic spines were a prominent phenotype in USP7-deficient neurons, we knocked down the select candidate substrates of USP7 using lentiviral transduction of shRNA in WT primary cortical neurons on DIV4 (validated in Figures S7A–S7E) and assessed their effects on dendritic spine density on DIV18 (Figures 6A–6G). Knockdown of the RNA-binding protein and splicing factor Ppil4 using two independent shRNAs significantly decreased spine density (Figures 6A–6D). Immunofluorescence analysis of PSD95, a major postsynaptic component of mature dendritic spines, confirmed the reduction of PSD95-positive spines in neurons subjected to Ppil4 knockdown (Figures 6A, 6E–6G, and S7F–S7H). These observations suggest that Ppil4 is required for the formation of mature, stable synapses. Surprisingly, knockdown of Trip12, a ubiquitin ligase associated with intellectual disability,[27,28] led to an increase in spine density (Figures 6B–6G and S7F–S7I). Knockdown of other candidate USP7 substrates had little to no effect on spine density (Figures 6B–6G and Figures S7F–S7I). Taken together, these results suggest that Ppil4 is required for synapse formation and/or maintenance in cortical neurons and that depletion of Ppil4 is sufficient to phenocopy the effects of USP7 loss.

Because several candidate substrates and their associated complexes were identified in our prior IP-MS experiments to interact with the USP7 TRAF domain, we tested whether these proteins also interact with full-length USP7. Therefore, we used HEK293T cells to express USP7 fused with streptavidin-binding peptide and a FLAG tag (SFB) prior

to pull-down with streptavidin beads (Figure 6H). Immunoblot detection of endogenous candidate substrates showed that Trip12, Smarcal1, Ubxn7, Ppil4, Ring1, and Fam172a co-precipitated with full-length USP7. Trip12 and Ppil4 displayed the most robust interaction with USP7, as demonstrated by their enrichment in the pull-down fraction compared to input lysate. Focusing on Ppil4, coIP with an antibody against Ppil4 demonstrated that endogenous Ppil4 interacted with GFP-tagged USP7 in HEK293T cells (Figure 6I). We then confirmed the interaction between endogenous USP7 and Ppil4 by performing reciprocal immunoprecipitation with separate antibodies against USP7 and Ppil4 in mouse brain lysates (Figure 6J). Together, these results demonstrate the interactions of full-length USP7 with several candidate substrates, including the RNA splicing factor Ppil4.

We next asked whether Ppil4 is a direct biochemical target of USP7-mediated deubiquitination. Using the tandem ubiquitin binding entities (TUBE),[29] an affinity matrix that specifically binds polyubiquitinated proteins, we purified endogenous polyubiquitinated proteins on DIV5 from lysates of *Usp7*$^{fl/fl}$; *Trp53*$^{+/-}$ cortical neurons expressing Cre. Subsequent immunoblot analyses showed that, compared to catalytically dead Cre, expression of WT Cre triggered a dramatic increase of high-molecular-weight forms of Ppil4 after proteasome inhibition, indicating ubiquitination of Ppil4 upon USP7 loss (Figure 6K). In an *in vitro* cell-free system, recombinantly expressed and purified USP7 also deubiquitinated FLAG-Ppil4 that had been immunopurified from HEK293T cells (Figures 6L and 6M). These observations demonstrate that Ppil4 is a *bona fide* target of USP7 deubiquitinase activity and that USP7 and Ppil4 collaboratively regulate the formation of dendritic spines and synapses of glutamatergic neurons (Figure 6P).

Last, to examine the relevance of Ppil4 as a USP7 substrate in the context of HAFOUS, we asked whether disease-associated *USP7* mutations disrupt the USP7-Ppil4 signaling pathway. By transfecting streptavidin-binding peptide-fused USP7 constructs (SB-USP7) carrying patient mutations,[30–33] 10 USP7 patient mutants were stably expressed in HEK293T cells. Subsequent immunoblot analyses showed that these patient mutants or catalytically dead USP7 (C223A) reduced the abundance of endogenous Ppil4 relative to WT USP7 (Figures 6N and 6O). These results suggest that disease-associated USP7 mutations in HAFOUS destabilize Ppil4.

USP7 regulates RNA splicing of synaptic genes in the cerebral cortex

Our concordant findings that the USP7 TRAF domain interacts with the spliceosome in neurons and that USP7 deubiquitinates the splicing factor Ppil4 to regulate dendritic spinogenesis led us to interrogate the role of USP7 in RNA splicing. We analyzed the transcriptome of the cerebral cortex of *Usp7* cKO; *Trp53*$^{+/-}$ and *Usp7* WT; *Trp53*$^{+/-}$ mice on P18 (Figure 7A). Sequenced RNA reads were first aligned and quantified for gene-level analysis (Figure S8A). Fold changes of RNAs upon USP7 loss, as determined by RNA sequencing (RNA-seq) analysis, and fold changes of proteins, as determined by our prior *in vivo* TMT-MS (Figures 3A–3D), were correlated only weakly (Figure S8B), suggesting that USP7 regulates RNA and protein through distinct mechanisms.

To characterize RNA splicing in *Usp7* cKO; *Trp53*$^{+/-}$ mice, we first employed LeafCutter analysis[34] by aligning RNA-seq reads to exon-exon junctions and identifying splicing

clusters (groups of exon-exon junctions sharing splice sites). Of 10,793 identified splicing clusters, 674 exhibited differential splicing between *Usp7* cKO; *Trp53*$^{+/-}$ and *Usp7* WT; *Trp53*$^{+/-}$ mice (false discovery rate [FDR] < 0.05). Because exon 6 of *Usp7* is flanked by *loxP* sites,[15] skipping of this exon ranked among the most significant differential splicing clusters in *Usp7* cKO; *Trp53*$^{+/-}$ mice (Figures S9A and S9B). Strikingly, genes of differential splicing clusters showed strong enrichment in synapse-related GO terms, indicating that USP7 regulates RNA splicing of synaptic genes in the cerebral cortex (Figure 7B). These differential splicing clusters included a slightly higher percentage of cryptic splicing clusters containing unannotated exon-exon junctions than nondifferential splicing clusters (Figure S8E). Concordantly, the cumulative distribution of cryptic splicing clusters was skewed toward low FDR (high $-\log_{10}$ FDR) compared to fully annotated splicing clusters (Figure 7C), indicating that USP7 loss promotes more cryptic splicing. The breakdown of exon-exon junction subtypes within differential splicing clusters compared to nondifferential splicing clusters showed higher percentages of junctions with only cryptic 5′ splice sites and junctions with both cryptic 5′ and 3′ splice sites but not junctions with only cryptic 3′ splice sites (Figure 7D), indicating that USP7 facilitates the selection of 5′ splice sites.

As an independent assessment of RNA splicing, we performed orthogonal analysis using DEXseq,[35,36] which aligns RNA-seq reads to counting bins (the smallest spliced unit) of individual exons, and quantitated usage of individual exons. Differential exon usage analysis between *Usp7* cKO; *Trp53*$^{+/-}$ and *Usp7* WT; *Trp53*$^{+/-}$ mice yielded 257 differential counting bins (FDR < 0.05) in 173 genes, including the expected downregulation of exon 6 of *Usp7* in *Usp7* cKO; *Trp53*$^{+/-}$ mice (Figure S8F). Consistent with LeafCutter analysis, genes of these differential exons were enriched in synapse-related GO terms, including postsynaptic density (Figure S8G). Thus, our exon usage analysis via DEXseq also supports that USP7 regulates the RNA splicing program of synaptic genes.

Next, we further characterized how specific genes are aberrantly spliced in the cerebral cortex of *Usp7* cKO; *Trp53*$^{+/-}$ mice. *Stxbp1*, which encodes the presynaptic protein Munc18–1, has two isoforms (Munc18–1a and Munc18–1b) in the mammalian brain, which differ by skipping or inclusion of exon 19[37] (Figure 7E). Alternative splicing of the two isoforms has been implicated in basic synapse function and dementia.[38,39] LeafCutter analysis detected increased inclusion of exon 19 of *Stxbp1* in the cerebral cortex of *Usp7* cKO; *Trp53*$^{+/-}$ mice (Figure 7F). We confirmed this effect using isoform-specific RT-qPCR (Figure 7G) with two primer sets that anneal to exon 19 of *Stxbp1* and the junction connecting exons 18 and 20 (Figure S9G). Importantly, peptide analysis of our *in vivo* TMT-MS data (Figures 3A–3D) also showed a significant increase of the peptide mapped uniquely to exon 19 of Munc18–1a but not Munc18–1b. In contrast, sequence-exclusive peptides, which are mapped to Munc18–1b but not Munc18–1a, did not consistently increase in *Usp7* cKO; *Trp53*$^{+/-}$ mice (Figure 7H).

We also examined alternative usage of exon 34b of the *Kalrn* gene, which produces a truncated isoform known as Kalirin-7. Kalirin-7 is highly enriched in the postsynaptic density[40] and has been shown to regulate dendritic spinogenesis and synaptic function in cortical neurons.[41,42] LeafCutter analysis demonstrated decreased usage of exon 34b

of *Kalrn* relative to the mutually exclusive exon 34a, suggesting an aberrant splicing mechanism decreasing Kalirin-7 in *Usp7* cKO; *Trp53*$^{+/-}$ mice (Figure 7J). This specific reduction of exon 34b was also detected using isoform-specific RT-qPCR (Figure 7K) and by examining the Kalirin-7-specific peptide in the TMT-MS data of the cerebral cortex (Figure 7L).

Last, one of the most significant differential splicing clusters in LeafCutter analysis was decreased inclusion of exon 1c of *Rtn4* in *Usp7* cKO; *Trp53*$^{+/-}$ mice (Figures S9C and S9D). Rtn4 encodes the membrane protein NOGO, whose alternative splicing at its C terminus generates functionally distinct isoforms, including the neurite- and synapse-suppressing canonical isoform NOGO-A.[43] Preferential usage of exon 1c over exon 3 generates the shortest isoform, NOGO-C, which was confirmed to decrease upon USP7 loss in both isoform-specific RT-qPCR (Figure S9E) and TMT-MS peptide analysis (Figure S9F). Together, these findings demonstrate that USP7 loss perturbs alternative splicing of *Stxbp1*, *Kalrn*, and *Rtn4*.

DISCUSSION

In this study, through a combination of unbiased omics experiments followed by targeted biochemical and functional characterization, we uncover several molecular and cellular mechanisms by which ubiquitin signaling controls brain development. In the process, we identify crucial roles of the deubiquitinase USP7 and generate important insights into the pathogenesis of HAFOUS. Extensive behavioral analyses demonstrate that conditional knockout of *Usp7* in glutamatergic neurons in mice recapitulate the major clinical features in HAFOUS, including impaired vision, motor performance, and cognition, in addition to the unusual aggressive phenotype. These findings suggest that loss of USP7 function in glutamatergic neurons in the forebrain might be relevant to HAFOUS.

In developmental studies, USP7 deletion causes p53-dependent apoptosis in post-mitotic glutamatergic neurons. Although the USP7-p53 axis has been characterized extensively in cancer cells,[10,11,44] our findings broaden the relevance of this signaling pathway to post-mitotic neurodevelopment. Nevertheless, our findings that most behavioral deficits of *Usp7* cKO mice persist following co-deletion of p53 indicate that the regulation of USP7 on glutamatergic neurodevelopment is predominantly p53 independent.

In an effort to define p53-independent molecular mechanisms of USP7 in glutamatergic neurons, we discover that several ribonucleoproteins and the spliceosome not only physically interact with the USP7 TRAF domain but also covary in USP7-deficient cortical neurons in our network analysis. Further proteomic and biochemical analyses have identified the RNA splicing factor Ppil4 as a new substrate of USP7, which is one key finding of this study. Importantly, subsequent transcriptomic analyses in the cerebral cortex reveal a disrupted RNA splicing program upon USP7 loss, especially aberrant usage of cryptic 5′ splice sites. Concordantly, recent mechanistic studies demonstrate that Ppil4 facilitates catalytic activation of the spliceosome right before the nucleophile attack of the 5′ splice site.[45,46] Future studies will be necessary to determine the molecular details of how USP7 regulates RNA splicing in neurons.

Our RNA splicing analysis also reveals that synaptic genes are strongly overrepresented in genes of differential splicing upon USP7 loss. Morphologic analyses show that loss of USP7 or Ppil4 reduces the density of dendritic spines in cortical neurons. These results support that USP7 and Ppil4 operate convergently to regulate the RNA splicing program of synaptic genes and synapse development. Because alternative splicing in synaptic genes is a prominent feature of the neuronal transcriptome that is required for the function of many synaptic proteins, including adhesion molecules and scaffold proteins,[47–49] it will be critical in future studies to test how synaptic physiology and function may be dysregulated in mouse or human neuron models with genetic manipulation of USP7 and Ppil4. Because abnormalities of synapse development are thought to underlie the pathogenesis of neurodevelopmental disorders of cognition,[50–52] synaptic regulation by USP7-Ppil4 signaling may play a key role in the pathogenesis of HAFOUS.

Through a series of analyses on the interactome of USP7 and proteomic dynamics upon acute depletion of USP7, we provide an actionable and unbiased framework to study deubiquitinases, facilitating both identification of specific substrates and characterization of proteome-wide mechanisms of deubiquitinases. Although there are methods of ubiquitin proteomics to characterize substrates of ubiquitin ligases,[4,53,54] to our knowledge, our study represents the first comprehensive characterization of potential substrates of a deubiquitinase in neurons. A notable finding from our analyses is that multiple ubiquitin ligases interact with USP7 and that their protein abundances are reduced upon USP7 loss. Ubiquitin ligases characteristically undergo self-ubiquitination and self-degradation.[11,55,56] Hence, USP7 might function as a positive regulator of these ubiquitin ligases by limiting their self-ubiquitination and degradation. Failure to rescue ubiquitin ligases from proteasomal degradation upon USP7 loss could potentially induce elevation of substrates of these ligases, perhaps accounting for many up-regulated proteins in the USP7 knockout brain (Figure 3B). Interestingly, among these ubiquitin ligases, Trip12 and Huwe1 are both associated with intellectual disability,[27,28,57,58] suggesting that the regulation of these ubiquitin ligases by USP7 may bear potential relevance to HAFOUS. Furthermore, our proteomic and biochemical analyses have also identified several chromatin and transcription regulators as novel candidate substrates of USP7 in neurons. In particular, the SWI/SNF chromatin remodeling enzyme Smarcal1 interacts with USP7 and is stabilized by USP7, suggesting a role for USP7 in regulating chromatin accessibility.

In conclusion, we elucidated the roles and mechanisms of the HAFOUS protein USP7 in the mammalian brain. Multiple lines of evidence demonstrate that USP7 regulates fundamental aspects of neurobiology via p53-dependent and predominantly p53-independent mechanisms, including the novel USP7-Ppil4 ubiquitin link. Beyond advancing our understanding of the major deubiquitinase USP7 in brain development, our study provides clues for the identification of biomarkers and potential treatments for patients with HAFOUS.

Limitations of the study

Although our study significantly advances our understanding of the functions and mechanisms of USP7 in the developing mammalian brain, limitations should be considered.

It remains unclear whether the observed changes on dendritic spines mechanistically result from decreased generation or increased pruning. Importantly, the scope of our study is limited to mechanisms of USP7 signaling in the cerebral cortex and did not address the heterogeneity in neuronal connectivity at the circuit level, which might be relevant to patients with HAFOUS. Although we extensively characterized the effect of p53 deletion on behavioral deficits in *Usp7* cKO mice, how USP7-Ppil4 signaling might trigger behavioral deficits was not explored due to a lack of genetic models of Ppil4 *in vivo*. In the mechanistic studies, although our screen revealed Ppil4 as a key target of USP7, we were not able to test every candidate substrate from our proteomics results due to antibody unavailability. Moreover, ubiquitination influences protein degradation as well as other aspects of protein function independent of protein turnover.

RESOURCE AVAILABILITY

Lead contact—Further information can be requested from the lead contact, Albert H. Kim (alberthkim@wustl.edu).

Materials availability—Materials generated in this study are available to researchers who are interested.

Data and code availability—The proteomics datasets (IP-MS and *in vivo* and *in vitro* TMT-MS) were deposited at ProteomeXchange PRIDE: PXD043225, PXD043848, and PXD043849, and the RNA-seq datasets were deposited at NCBI Gene Expression Omnibus: GSE280944, both of which are publicly available upon publication. This paper does not report original code. Any additional information required to reanalyze the data in this paper is available from the lead contact upon request.

STAR★METHODS

EXPERIMENTAL MODEL AND STUDY PARTICIPANT DETAILS

Mice—Animals were cared for in accordance with NIH guidelines. All experimental methods were approved by Washington University Institutional Committee on the Use and Care of Animals under the protocol numbers 20180303 and 210083. Animals were housed in a 12:12 light:dark cycle. We employed trio breeding and only used unaffected animals as parents. Pups were weaned from P21 to P28 and genotyped by phenol/chloroform DNA extraction of tail or toe (<P7 pups) biopsy followed by PCR. Weaned mice were separated by sex and relocated for breeding from 6 to 24 weeks' old. Animals were allocated to experimental versus control groups based on genotype. Sex matched-littermate controls were used in all experiments, and the age at which animals were used is reported in figures or legends.

The *Usp7* floxed mice were first obtained on C57BL/6J and 129Sv mixed background[15] and then backcrossed to C57BL/6J background with speed congenics (last generation SNP typing >99% determined by Dartmouse). The *NEX-cre* mice on C57BL/6J background were obtained from Dr. Hui-Chen Lu's lab in Indiana University Bloomington, under the permission of Dr. Sandra Goebbels.[19] Only the videotaped *Usp7* cKO mice were generated

from the *Usp7* floxed mice on C57BL/6J and 129Sv mixed background while the mice in all experiments were generated from C57BL/6J mice and maintained on C57BL/6J background. *Usp7* cKO mice were separated and single-caged once they were found to bite their cage mates.

The *Trp53* mutant mice on C57BL/6J background were purchased from the Jackson Laboratory (Cat#002101). Consistent with the description from the Jackson Laboratory, female $Trp53^{-/-}$ mice were born under the Mendelian ratio and exhibited young adult lethality. Therefore, only male mice with $Trp53^{-/-}$ were used for breeding and in vivo experiments. For cortical neuron culture, $Usp7^{fl/fl}$; $Trp53^{-/-}$ male mice crossed with either $Usp7^{fl/fl}$; $Trp53^{-/-}$ or $Usp7^{fl/fl}$; $Trp53^{+/-}$ female mice to produce embryos with $Usp7^{fl/fl}$; $Trp53^{-/-}$ or $Usp7^{fl/fl}$; $Trp53^{+/-}$. As p53 deficiency increases the propensity to grow tumor, mice and embryos with observed tumor bumps were checked and excluded from all experiments.

The wild-type CD1 mice with timed E16 pregnancy for the *in vitro* apoptosis analysis, and the Long-Evans rat with timed E17 pregnancy for the IP-MS analysis were both purchased from Charles River. No breeding was performed with these animals.

HEK293T cell line—Human embryonic kidney 293T (HEK293T/HEK293LE; Clontech 632180) cells were cultured in DMEM with 10% fetal bovine serum (Fisher #10082–147) and penicillin/streptomycin (Life Technologies #15140122). For lentiviral packaging, DNA/PEI (Polysciences) complexes were suspended in Opti-MEM medium (Gibco) and transfected into HEK293T cells with about 80% confluency. The transfer plasmid was mixed with packaging plasmid psPAX2 and envelope plasmid pCMV-VSVG. The medium was replaced on the next day and the new medium containing lentivirus was collected after 3 days. Cell debris was filtered out from the collected medium and Lenti-X Concentrator (Clontech) was then used to precipitate the lentivirus in the medium. After incubation at 4°C overnight to 3 days, virus-containing pellets were collected by centrifuging at 1500g for 45 min at 4°C, resuspended in phosphate-buffered saline (PBS), and stored at −80°C in aliquots.

Cortical neuron culture—For IP-MS and immunocytochemistry of USP7 TRAF domain, cortical neurons were cultured from E17 Long-Evans rat embryos. Rat rather than mouse neurons were used in this experiment to maximize depth of mass spectrometry analysis with affinity-purified lysates. For *in vitro* apoptosis analysis, cortical neurons were cultured from wild-type E16 CD1 mouse embryos because CD1 mice produce bigger litter and more neurons than C57BL/6L mice. For dendrite morphology analysis and TUBE assay, cortical neurons were cultured from E15 $Usp7^{fl/fl}$; $Trp53^{+/-}$ embryos on C57BL/6J background. For *in vitro* TMT proteomics, cortical neurons were cultured from E15 $Usp7^{fl/fl}$; $Trp53^{-/-}$ embryos on C57BL/6J background. For spine analysis with RNAi knockdown, cortical neurons were cultured from E15 C57BL/6J wild-type embryos.

To prepare cortical neurons (previously described as Spiegel et al. 2014[62]), embryonic cortices were dissected in 1X HBSS and digested with 2.5% Trypsin (Gibco) at 37°C. DNase (Roche) was added to digest free-floating DNA from dead cells. Trypsin-digested

tissue was further triturated with pipette acid to fully dissociate cells. Dissociated neurons were seeded onto tissue culture dishes pre-coated with poly-L-lysine (0.1 mg/mL) at a density of 1.2×10^5 cells/cm^2. Neurons were first cultured with neurobasal medium with 1% fetal bovine serum (2% for rat neuron), 0.5mM glutamine, B27 Supplement (Gibco) and penicillin/streptomycin (Life Technologies #15140122) at 37°C with 5% CO_2. On DIV4, DIV8 and DIV12, neurons were fed with half fresh medium without serum. Every day after DIV14, one-fifth of the old medium was replaced with fresh medium without serum to maintain stable medium composition. Neuron viability was confirmed on DIV11 with MTS assay.

METHOD DETAILS

General design of behavioral tests—Behavioral tests were conducted in the Washington University Animal Behavior Core and are approved by the Washington University Institutional Animal Care and Use Committee. Sex and litter-matched mice with and without p53 heterozygosity were tested separately due to limit of cohort size for each batch of phenotypical analysis. Total number of animals used for behavioral tests are: A cohort of 29 *Usp7* cKO mice (15 females, 14 males) was tested for tail-biting behavior (Figures 1J and 1K). Another cohort of 7 *Usp7* WT mice (5 females, 2 males), 9 *Usp7* cHet mice (6 females, 3 males), 8 *Usp7* cKO mice (6 females, 2 males) was used in all behavioral tests and body weight measurements (Figures 1C–1I and S1C–S1K). A cohort of 33 *Usp7* cKO; *Trp53*$^{+/-}$ mice (12 females, 21 males) was tested for tail-biting behavior. Anorther cohort of 13 *Usp7* WT; *Trp53*$^{+/-}$ mice (2 females, 11 males), 8 *Usp7* cHet; *Trp53*$^{+/-}$ mice (2 females, 6 males), 15 *Usp7* cKO; *Trp53*$^{+/-}$ mice (2 females, 13 males) was tested for visual acuity (VOS test) and fear conditioning (Figures 2E and 2I–2K). A third cohort of 10 *Usp7* WT; *Trp53*$^{+/-}$ mice (4 females, 6 males), 14 *Usp7* cHet; *Trp53*$^{+/-}$ mice (6 females, 8 males), 10 *Usp7* cKO; *Trp53*$^{+/-}$ mice (4 females, 6 males) were used for all other behavioral tests and body weight measurements (Figures 2F–2H, S3B, and S3D–S3J). A separate cohort of 12 *Trp53*$^{+/-}$ mice and 11 *Trp53*$^{+/+}$ mice were tested for visual acuity and fear conditioning (Figures S3C and S3K–S3M). After the event that any one genotype of mice within a specific litter were all accidentally dead or wounded resulting from presumed fighting among co-caged mice, all mice in the litter were removed from the analysis to reassure all animals are still litter-matched. All tests were performed during the light phase of the light/dark cycle by a female experimenter blind to the genotypes. Mice were acclimated to the test room for 30 min prior to testing.

Sensorimotor battery—Ledge, platform, pole, and inverted screen tests were performed to assess sensorimotor function. Time in each task was manually recorded. The average for two trials was used for analyses. Test duration was 60s, except for the pole test, which was extended to 120s. For walking initiation, time for an animal to leave a 21 × 21cm square on a flat surface was recorded. For ledge and platform tests, the time the animal was able to balance on an acrylic ledge (0.75cm wide and 30cm high), and on a wooden platform (1.0cm thick, 3.0cm in diameter and elevated 47cm) was recorded, respectively. The pole test was used to evaluate fine motor coordination by quantifying time to turn 180° and climb down a vertical pole. The screen tests assessed a combination of coordination and strength

by quantifying time to climb up or hang onto a mesh wire grid measuring 16 squares per 10cm, elevated 47cm and inclined (60° or 90°) or inverted.

Catwalk—Natural gait parameters were measured using the CatWalk XT gait analysis system (Noldus, Inc). Mice were habituated to the apparatus and testing room the day before testing by placing each mouse on the glass walkway for 5 min to help facilitate movement during the test session. Testing was conducted with the room lights off. The following day, mice were placed on the 8-cm wide glass walkway and allowed to walk naturally until 3 recordings were collected meeting compliance criteria of less than 60% speed variability. A camera below the glass surface recorded the paw placement and intensity of each paw as the mouse moved across the walkway. Run speed, swing speed, stride length, and mean intensity of paw placement were analyzed to assess differences in gait.

Virtual optomotor system (VOS)—Visual acuity was assessed by recording Spatial frequency thresholds, in cycles per degree (c/d) using the mouse OptoMotry HD System (Cerebral Mechanics Inc.). This is a virtual-reality system designed to quantify visuomotor behavior.[63] Mice were allowed to acclimate to procedure room 30 min prior to testing. Each mouse was placed onto a platform in the center of the VOS chamber, and the experimenter tracked the movement of the animal's head during the course of the test. VOS chamber consists of four computer screens surrounding the platform with a camera to capture the OMR from above. Drift speed was set at 12.5, contrast 100°. The OptoMotry software uses a staircase method to determine at which threshold the optomotor reflex (OMR) is no longer detected by the experimenter. Experimenter remained blind to the direction of virtual movement.

Spontaneous alternation Y-maze—Testing was conducted according to our previously published procedures.[64] Briefly, this involved placing a mouse in the center of a Y-maze that contained three arms that were 10.5 cm wide, 40 cm long and 20.5 cm deep where an arm was oriented at 120° with respect to each successive other arm. Mice were allowed to explore the maze for 8 min and entry into an arm was scored only when the hindlimbs had completely entered the arm. An alternation was defined as any three consecutive choices of three different arms without re-exploration of a previously visited arm. The number of alternations and arm entries along with the percentage of alternations, which was determined by dividing the total number of alternations by the total number of entries minus 2, then multiplying by 100 was analyzed as a measure of spontaneous alternation.

Acoustic startle response/auditory function—Acoustic startle responses were measured using Kinder Scientific Startle Reflex equipment and software (Kinder Scientific, Inc) Auditory function was assessed by measuring startle response to auditory stimuli pulses (40 ms broadband burst) presented at 80dB, 90dB, 100dB, 110dB, and 120dB above background noise (65dB). Each trial type was presented 10 times in a random order over a 20 min session, with inter-trial-intervals ranging from 5 to 15 s between trials. Beginning at stimulus onset, 1 ms force readings were obtained to record an animal's startle amplitude. The average force response to each sound pressure level was analyzed as a measure of auditory function.

Conditioned fear—Two distinct chambers were used to train and test mice (26 × 18 × 18 cm high) (Med-Associates, St. Albans, VT) which were easily distinguished by different olfactory, visual, and tactile cues present in each chamber. On day 1, each mouse was placed into the conditioning chamber (peppermint odor) for 5 min and freezing behavior was quantified during a 2 min baseline period. Freezing (no movement except that associated with respiration) was quantified using FreezeFrame image analysis software (Actimetrics, Evanston, IL) which allows for simultaneous visualization of behavior while adjusting for a "freezing threshold" during 0.75 s intervals. After baseline measurements, a conditioned stimulus (CS) consisting of an 80 dB tone (white noise) was presented for 20 s followed by an unconditioned stimulus (US) consisting of a 1 s, 1.0 mA continuous foot shock. This tone-shock (T/S) pairing was repeated each minute over the next 2 min, and freezing was quantified after each of the three tone-shock pairings. Twenty-four hours (h) after training, each mouse was placed back into the original conditioning chamber to test for fear conditioning to the contextual cues in the chamber. This involved quantifying freezing over an 8 min period without the tone or shock being present. Twenty-four h later, the mice were evaluated on the auditory cue component of the conditioned fear procedure, which included placing each mouse into the other chamber containing distinctly different cues (coconut odor). Freezing was quantified during a 2 min "altered context" baseline period as well as over a subsequent 8 min period during which the auditory cue (CS) was presented. Shock sensitivity was evaluated following completion of the conditioned fear test.

Tail-biting behavior—To quantitate biting behavior, *Usp7* cKO or *Usp7* cKO; *Tp53*$^{+/-}$ mice were weaned after 3 weeks old and co-housed with their littermates. Male and female mice were separated and housed in a regular 12:12 light:dark cycle. Tail wounds were checked every week until 12 weeks old. Once tail wounds were found, the aggressors were marked and separated to avoid more biting. Victim mice with severe tail wound were euthanized and photographed. To video record the biting behavior, P33 aggressor and littermate were placed onto an ice cream box lid for free exploration.

Calcium phosphate sparse transfection—Primary cortical neurons were transfected as previously described.[65] Briefly, transfection mix was prepared by mixing 50 ng/μL plasmid DNA, 0.25mM $CaCl_2$ and HEPES Buffered Saline (Invitrogen) and the DNA-calcium phosphate precipitate was made by pipetting up and down 10 times. Neurons were washed 3 times and starved with fresh serum-free medium at 37°C for 30min, and then 40μL of the transfection mix was dropped into each well in a 24-well plate (80μL for 12-well plate) and incubate at 37°C for 20–30 min. To remove DNA-calcium phosphate precipitate and avoid toxicity, neurons were then washed with fresh serum-free medium 3 times again and put back conditioned medium.

Immunofluorescence and immunocytochemistry—For immunofluorescence, mice were anesthetized with isoflurane, perfused with 0.1% heparin in PBS and 4% paraformaldehyde (>P5) or decapitated without perfusion (<P5) before brain dissection and immersion fixation of the whole brain in 4% paraformaldehyde overnight at 4°C. Fixed brains were then placed in 30% sucrose in PBS for cryopreservation. After sinking in the sucrose solution, the brains were embedded with mixture of O.C.T. Compound (Sakura

Finetek) and 30% sucrose solution (3:7), flash-frozen using liquid nitrogen. With a Leica cryostat, the frozen brains were sectioned at 16μm thickness and placed onto positively charged slides. For spine analysis, the brains were sectioned at 100μm thickness and placed into FD section storage solution (FD NeuroTechnologies). For immunocytochemistry, cells were initially seeded onto HNO_3-treated coverslips in 12 or 24 well-plates, washed with warm PBS and fixed in 4% paraformaldehyde for 30min on ice. For staining, brain sections or fixed cells were washed with PBS, permeabilized with 0.4% Triton X-100 and blocked with 3% Bovine serum alumin (BSA) and 10% goat serum. The permeabilized and blocked sections or cells was incubated with primary antibody overnight at 4°C, followed by incubation with fluorescence-conjugated secondary antibodies (Invitrogen) for 2 h at room temperature and Hoechst diluted in PBS at 1:2000. The stained sections or cells were mounted onto slides with Fluoromount-G (SouthernBiotech) or Prolong Glass Antifade Mountant (Invitrogen) for spine imaging. Antigen retrieval with citrate acid (0.1 M, pH 6.8 with 0.1% Tween 20) for 15 min boiling prior to blocking was required for labeling with anti-Ki67 antibody.

***In vivo* apoptosis analysis—**Cryosections of P0 mouse brains were immunostained with anti-cleaved caspase-3 (c-cas-3) antibody (Cell Signaling #9961, 1:4000) for apoptosis analysis. Image acquisition and quantitation of the c-cas-3 intensity were blind to mouse genotypes at all steps below. 6–8 consecutive coronal sections per mouse, 3–5 mice per genotype were imaged with Leica DMi8 scanning microscope with instant computational clearing (THUNDER). The imaged sections were selected based on matched hippocampal morphologies across all mice. Segmentation of the cortex to analyze was performed based on Hoechst nuclei counterstain. C-cas-3 integral intensity within the segmented region of each section was measured with ImageJ and normalized to area.

***In vitro* apoptosis analysis—**Primary cortical neurons from E16 wild-type CD1 mouse embryos were sparsely transfected at DIV3 with U6 empty vector, or U6-driven plasmids of shRNAs targeting USP7 or irrelevant USP30 along with EGFP plasmids. The transfected neurons were fixed at DIV5, 6 and 7, immunolabeled with anti-*c*-cas-3 (Cell Signaling #9961) and anti-GFP antibody (Abcam #ab13970) and imaged with Zeiss Axio Imager Z2 with ApoTome 2. Image acquisition and quantitation were blind to groups at all steps. Apoptotic cells are counted as GFP+ cells with c-cas3 signal in the cell body and the intensity of apoptosis was quantitated by the percentage of apoptotic cells over all GFP+ cells. The analysis was repeated with three batches of neuron culture and 2–3 wells in 12-well plates were used per group for each culture.

Immunoblotting—Cells or cortical tissues were lysed in RIPA buffer (Cell Signaling #9806) or TNE buffer (50mM Tris pH 7.4, 100mM NaCl, 0.1mM EDTA, 1% NP40) mixed with protease inhibitor cocktail (Sigma #P8340). Total protein was quantified with Bradford reagent (Bio-Rad). Lysate samples were separated by SDS-PAGE or LDS-NuPAGE and transferred to 0.2μm nitrocellulose membrane (GE Healthcare) via tank immersion. Membranes were blocked in 5% non-fat Milk in Tris-buffered saline with 0.05% Tween 20 (TBST) at 4°C overnight or 2 h at room temperature, incubated with primary antibodies at 4C overnight, and subsequently with infrared fluorescent secondary

antibodies (LI-COR) for 2 h at room temperature. Washes with TBST three times were applied to membranes after every antibody incubation step. LI-COR Odyssey CLx imager and LI-COR Image Studio software were used to image the blot at 600 dpi and to determine fluorescence densitometry to quantitate relative protein abundance. The relative abundance of each protein was normalized to loading control proteins (14–3-3 or Lamin A/C) in the same lane. Exposure time was adjusted to avoid pixel saturation. For immunoblotting following co-immunoprecipitation with mouse brains, secondary antibody is replaced with Veriblot IP detection reagent (Abcam) to minimize non-specific signal.

Immunoprecipitation—For immunoprecipitation of GFP-TRAF domain, we generated total cell lysates from HEK293T cells with TNE lysis buffer as described above. 5μM proteasome inhibitor MG132 was applied to enhance the expression of Myc3-Mdm2 in HEK293T cells. 1.5μg rabbit anti-GFP antibody (homemade) was added to 200μL lysate at 2 μg/μL total protein concentration determined by Bradford reagent followed by rotation at 4°C overnight. After antibody binding, 18μL of PBS-washed protein G agarose beads (GE Healthcare) were added per immunoprecipitation. Bead binding proceeded for 1 h at 4°C before 3 times wash with TNE lysis buffer and 3 times wash with cold PBS. 30μL LDS sample buffer was added to beads per immunoprecipitation and heated at 70°C for elution. The precipitated proteins were proceeded to immnunoblot analysis.

For endogenous immunoprecipitation, we generated total cell lysates from whole mouse brains of postnatal day 4 with TNE lysis buffer. 4μg Rabbit anti-Ppil4 (Bethyl) or Rabbit anti-USP7 antibody (Bethyl) or Rabbit normal IgG control (Cell Signaling) was added to 200μL lysate at 4 μg/μL total protein concentration determined by Bradford reagent followed by rotation at 4°C overnight. After antibody binding, 16μL of PBS-washed protein A agarose beads (GE Healthcare) were added per immunoprecipitation. Bead binding proceeded for 1 h at 4°C before 3 times wash with TNE lysis buffer and 4 times wash with cold PBS. 30μL LDS sample buffer was added to beads per immunoprecipitation and heated at 70°C for elution. The precipitated proteins were proceeded to immunoblotting analysis.

For immunoprecipitation of FLAG-TRAF domain, we generated total neuron lysates from primary rat neurons with the TNE lysis buffer. pHAGE-hSyn-TRAF WT/RDW were transduced into neurons at DIV7 and protein lysates were harvested at DIV10. 20μL PBS-washed M2 anti-FLAG agarose beads (Sigma) were added to 2.5mL lysate at 2 μg/μL total protein concentration for 3 h incubation at 4°C. The beads were washed 3 times with TNE lysis buffer, 3 times with cold PBS, followed by 3 times wash with 200 ng/μL 3x FLAG peptides (APExBio) for elution. 1.5% eluted samples were used for LDS-NuPAGE followed by silver stain (Invitrogen) while the rest was proceeded to tricarboxylic acid (TCA) precipitation and LC-MS/MS analysis. 3 biological replicates of neuron plates with TRAF WT and RDW mutant were used.

LC-MS/MS identification of interactors of the USP7 TRAF domain—We resuspended the sample in 20 μL of 8 M urea, 100 mM EPPS pH 8.5. We added 5mM TCEP and incubated the mixture for 15 min at room temperature. We then added 10 mM of iodoacetamide for 15 min at room temperature in the dark. We added 15 mM DTT

to consume any unreacted iodoacetamide. We added 180μL of 100 mM EPPS pH 8.5. to reduce the urea concentration to <1 M, 1 μg of trypsin, and incubated at 37°C for 6 h. The solution was acidified with 2% formic acid and the digested peptides were desalted via StageTip, dried via vacuum centrifugation, and reconstituted in 5% acetonitrile, 5% formic acid for LC-MS/MS processing.

Mass spectrometry data were collected using a Q Exactive mass spectrometer (Thermo Fisher Scientific, San Jose, CA) coupled with a Famos Autosampler (LC Packings) and an Accela600 liquid chromatography (LC) pump (Thermo Fisher Scientific). Peptides were separated on a 100 μm inner diameter microcapillary column packed with ~20 cm of Accucore C18 resin (2.6 μm, 150 Å, Thermo Fisher Scientific). For each analysis, we loaded ~1 μg onto the column. Peptides were separated using a 75 min method from 2 to 25% acetonitrile in 0.125% formic acid with a flow rate of ~300 nL/min. The scan sequence began with an Orbitrap MS^1 spectrum with the following parameters: resolution 70,000, scan range 300–1500 Th, automatic gain control (AGC) target 1×10^5, maximum injection time 250 ms, and centroid spectrum data type. We selected the top twenty precursors for MS^2 analysis which consisted of HCD high-energy collision dissociation with the following parameters: resolution 17,500, AGC 1×10^5, maximum injection time 90 ms, isolation window 1.6 Th, normalized collision energy (NCE) 27%, and centroid spectrum data type. The underfill ratio was set at 9%, which corresponds to a 1.5×10^5 intensity threshold. In addition, unassigned and singly charged species were excluded from MS^2 analysis and dynamic exclusion was set to automatic.

Mass spectra were processed using a SEQUEST-based in-house software pipeline. MS spectra were converted to mzXML using a modified version of ReAdW.exe. Database searching included all entries from the rat uniprot database which was concatenated with a reverse database composed of all protein sequences in reversed order. Searches were performed using a 50 ppm precursor ion tolerance. Product ion tolerance was set to 0.03 Th. Carbamidomethylation of cysteine residues (+57.0215Da) were set as static modifications, while oxidation of methionine residues (+15.9949 Da) was set as a variable modification. Peptide spectral matches (PSMs) were altered to a 1% FDR.[66,67] PSM filtering was performed using a linear discriminant analysis, as described previously,[68] while considering the following parameters: XCorr, ΔCn, missed cleavages, peptide length, charge state, and precursor mass accuracy. Peptide-spectral matches were identified, quantified, and collapsed to a 1% FDR and then further collapsed to a final protein-level FDR of 1%. Furthermore, protein assembly was guided by principles of parsimony to produce the smallest set of proteins necessary to account for all observed peptides.

TMT mass spectrometry

Sample preparation: Preparation of samples prior to mass spectrometry was performed as previously described.[69] In brief, 5 litter-matched female murine cortices were harvested and flash-frozen at P17 and then lysed by bead-beating in lysis buffer (200mM EPPS, pH 8.5 and 8 M urea with protease and phosphatase inhibitors) at maximum speed for four cycles of 30 s each, with 1 min pauses on ice between cycles. For 16-plex experiment, primary mouse cortical neurons were dissociated from E15 USP7 fl/fl; Tp53 −/− embryos

on C57BL/6J background. USP7 depletion was induced by lentiviral transduction of wild-type Cre recombinase or catalytically dead Cre as control at DIV3. Four biological replicates of neurons transduced with wild-type Cre and catalytically dead Cre were harvested at DIV6 and DIV8, respectively. For cultured neurons the lysate was passed 10 times through a 21-gauge (1.25 inches long) needle. An equal quantity of protein (100 μg) for each condition (10 cortex slices, 16 samples of transduced neurons) was reduced with 5 mM tris (2-carboxyethyl) phosphine (room temperature, 15 min) before proteins were alkylated with 10 mM iodoacetamide (room temperature, 30 min in the dark). Finally, excess iodoacetamide was quenched with 10 mM dithiothreitol (room temperature, 15 min). Alkylated proteins were isolated by methanol-chloroform precipitation prior to protease digestion. The samples were diluted in lysis buffer to a volume of 100 μL before adding methanol (400 μL), chloroform (100 μL) and water (300 μL) stepwise with vortexing after addition of each solvent. The samples were centrifuged for 1 min at 14,000 g and the aqueous and organic phases were removed, leaving only the protein disk, which was washed with methanol (500 μL) and centrifuged at 21,000 g for 2 min at room temperature. After removal of methanol supernatant, the samples were resuspended in 200 mM EPPS (pH 8.5) containing Lys-C protease (Wako) at a 100:1 protein-to-protease ratio then incubated overnight at room temperature while shaking. Trypsin was then added at a 100:1 protein-to-protease ratio, and the reaction was incubated 6 h at 37°C. Acetonitrile (30 μL) was added to the digested peptides and vortexed before adding 200 μg TMT reagent (TMT10 or TMTpro16) for a 2:1 TMT-to-peptide ratio. The samples were incubated at room temperature for 1 h and briefly vortexed every 10 min. Once labeling efficiency was confirmed, the reaction was quenched with hydroxylamine to a final concentration of 0.3% (v/v) for 15 min. The TMT-labeled samples were pooled, vacuum-centrifuged long enough to evaporate the acetonitrile, then desalted with a C18 solid-phase extraction (SPE) (Sep-Pak, Waters) and vacuum centrifuged to dryness.

Basic reversed-phase fractionation: For basic reversed-phase fractionation, desalted peptides were resuspended in Buffer A (10 mM ammonium bicarbonate, 5% ACN, pH 8), then subjected to a linear gradient from 13% to 42% of Buffer B (10 mM ammonium bicarbonate, 90% ACN, pH 8) on an Agilent 300Extend C18 column (3.5 μm particles, 4.6 mm ID and 250 mm in length). The peptide mixture was fractionated into a total of 96 fractions which were consolidated into 24 super fractions, of which, 12 non-adjacent samples were analyzed by the mass spectrometer. These 12 fractions were vacuum centrifuged until dry, then desalted via StageTip for LC-MS analysis.

LC-MS analysis: The LC-MS analysis and protein quantification was slightly different for proteins extracted from the mouse cortex slices versus those from the cultured neurons, reflecting changes in instrumentation over the course of these experiments. Eluted peptides were introduced to an Orbitrap Fusion with FAIMS pro (mouse cortex slices) or Orbitrap Fusion Lumos (cultured neurons) mass spectrometer coupled to a Proxeon EASY-nLC 1200 LC pump (both from ThermoFisher Scientific). Peptides were separated over a 90 min (cortex) or 120 min (neurons) gradient on a 35–40 cm long 100 mm inner diameter column packed with Accucore (2.6 μm, 150Å) resin (ThermoFisher Scientific). For cortex slices the FAIMS voltages were set at −40, −60, and −80V using a top speed method with 1s

per CV. Full MS spectra were acquired in the Orbitrap at a resolution of 120,000 and the 10 most intense MS1 ions were selected for MS2 analysis in the ion trap. The isolation width was set to 0.7 Da and isolated precursors were fragmented by CID at a normalized collision energy (NCE) of 35%, and a max injection time of 35 ms (cortex) or 50 ms (neurons). Following acquisition of each MS2 spectrum, for the murine cortex experiment, a synchronous precursor selection (SPS) MS3 scan was collected on the top 10 most intense ions in the MS2 spectrum. For the experiment from cultured neurons, a real-time search (RTS-MS3) strategy was used, where only those SPS ions (up to 10) matching a theoretical peptide spectrum were isolated for MS3 analysis. These SPS-MS3 precursors were fragmented by higher energy collision-induced dissociation (HCD) at an NCE of 65% (TMT10) or 50% (TMTpro) and analyzed using the Orbitrap at 50,000 resolution, with a max injection time of 100 ms (cortex) or 200 ms (neurons).

Database searching: Mass spectra were processed using SEQUEST (cortex) or Comet (neurons). Database searching included all entries from the murine Uniprot database downloaded 07/2014 (cortex) or 07/2020 (neurons). Searches were performed using a 50-ppm precursor ion tolerance for total protein-level analysis. The product ion tolerance was set to 0.9 Da (SEQUEST) or 1.005 (Comet). TMT tags (+229.163 Da) or TMTpro tags (+304.2071) on lysine residues and peptide N termini and carbamidomethylation of cysteine residues (+57.021 Da) were set as static modifications, while oxidation of methionine residues (+15.995 Da) was set as a variable modification. Peptide-spectrum matches (PSMs) were identified, quantified, and filtered to a 1% peptide false discovery rate (FDR) and then collapsed further to a final protein-level FDR of 1%. The total summed signal-to-noise (S:N) measurements of the peptides in each condition were used to calculate column normalization factors to account for small differences in sample abundance. Then, for each protein, signal-to-noise (S:N) measurements of the peptides were summed and then normalized to 100 across the all samples to yield a relative abundance measurement.

RNA extraction and RT-qPCR—Total RNA from mouse cortical tissues and primary cortical neurons was isolated using QIAshredder and RNeasy Plus Mini Kit (QIAGEN) according to the manufacturer's instructions. Cortical tissues were homogenized with mortar and pestle on dry ice during lysis. The extracted RNA was reverse-transcribed into cDNA by a High-Capacity cDNA Reverse Transcription Kit with RNase Inhibitor (Applied Biosystems). Mixed cDNA, designed primers and Power SYBR Green PCR Master Mix (Applied Biosystems) were loaded to qPCR on a CFX Connect Real-Time PCR Detection System (Bio-Rad). PCR program runs as below: hot start, 95°C for 10 min; amplification 40 cycles including denaturation (95°C for 15s), annealing (57°C for 30s), and extension (72°C for 30s). Melting curve analyses (65°C for 5s and then 5s each at 0.5°C increments between 65C and 95C) were conducted to ensure single-peak amplicon. Glyceraldehyde-3-phosphate dehydrogenase (GAPDH) was used as the internal reference control.

Streptavidin pull-down—For assessment of the interaction between USP7 and endogenously expressed proteins, an S protein-Streptavidin-binding peptide-FLAG (SFB)-tagged USP7 construct[61] (Addgene plasmid #99393) was transfected into HEK293T cells via PEI transfection. The lysate containing SFB-USP7 was generated with TNE lysis buffer

as described above and incubated with PBS-washed Dynabeads MyOne Streptavidin T1 beads (Invitrogen #65601) for 1 h at 4°C with rotation. Next, the beads were washed 3 times with TNE lysis buffer and 4 times with cold PBS, followed by LDS sample buffer elution. The eluted proteins were analyzed by immunoblotting along with 2% input lysates in the same blot.

Tandem ubiquitin binding entities (TUBE) assay—The TUBE assay was performed according to Tsao et al. 2021 with modification.[70] Briefly, primary cortical neurons from E15 mouse embryos were transduced with Cre wild-type (WT) or catalytically dead (CD) lentiviruses at DIV3 and treated with 10μM MG132 at DIV5. Neuron lysates were generated with TNE lysis buffer 16 h after MG132 treatment. Cold TBST-washed pan-selective TUBE 2 beads (LifeSensors #UM-0402M) were incubated with neuron lysates overnight at 4°C with rotation. Next, the beads were washed 5 times with cold TBST and 2 times with cold PBS, followed by LDS sample buffer elution. The eluted proteins were analyzed by immunoblotting along with 2% input lysates in the same blot.

***In vitro* deubiquitination assay—**For *in vitro* ubiquitination assay, HEK293T cells were transfected with pcDNA3.1-FLAG-Ppil4 plasmid. After the treatment of 10μM the proteasome inhibitor MG132 for 16 h, the cells were harvested, lysed with 1% NP40 TNE lysis buffer, and the FLAG-Ppil4 was purified by immunoprecipitation with M2 anti-FLAG agarose beads (Sigma) as described above. 20μL PBS-washed M2 beads were added to 2.5mL lysate at 2 μg/μL total protein concentration for 3 h incubation at 4°C. The beads were washed 3 times with TNE lysis buffer, 2 times with high-salt PBS buffer (0.5M NaCl) to reduce non-specific binding, and then 3 times with regular PBS. Then we resuspended the washed beads with deubiquitination buffer (50mM Tris-HCl, 150mM NaCl, 5mM $MgCl_2$ and 10mM DTT, final pH 7.3) and distributed 9μL beads for each deubiquitination reaction. Either 1μL 500nM recombinant His-USP7 (R&D system) or 1μL deubiquitination buffer as vehicle control was added to each reaction and incubated for 1 h at 37°C. LDS sample buffer was then added to stop the reaction and ubiquitinated Ppil4 was analyzed with immunoblotting. Densitometric analysis was performed with FLAG-Ppil4 purified from 3 biological replicates of HEK293T lysates. Ubiquitinated Ppil4 was quantified as the fraction of Ppil4 integral fluorescent intensity above the molecular weight of the lowest full-length Ppil4 (~65kD).

Diffusion-weighted *ex vivo* MRI and volumetric measurements—The skull of the fixed brain was removed before transferring to a 3-mL syringe containing fresh PBS. Diffusion-weighted MRI experiment was performed on 9.4-T Bruker scanner with a CryoProbe. Fifteen sagittal slices, centered at the midline (slice 8), were acquired to cover the entire brain. Twenty-five-direction diffusion-weighted measurements were performed using a spin-echo diffusion-weighting sequence with the following parameters: repetition time (TR) = 1.5 s; echo time (TE) = 32 ms; field of view (FOV) = 20 × 20 mm2; matrix size = 192 × 192 (zero-filled to 384 × 384), slice thickness = 0.6 mm, max; b value = 3,000 s/mm^2, Δ = 20 ms; δ = 5 ms; partial Fourier factor = 1.33; total scan time = 93.6 min. Diffusion-weighted data were converted to nifiti format followed by analysis using the lab-developed DBSI software package to perform DBSI multi-tensor

analysis.[71] DBSI-derived fiber fraction was used to reflect apparent axonal[72]/dendritic[73] density. DBSI-derived restricted and non-restricted fractions were used to estimate the extent of cellularity and vasogenic edema.[73] For volumetric measurement, segmentation was performed manually employing ITK-SNAP (version 3.8, www.itksnap.org).[74] The Allen Mouse Brain Atlas was used as a reference to identify cortex and hippocampus. The three parasagittal slices at each side of midline (slices 4–6 and 10–12) were used to segment cortex and hippocampus.

Adeno-associated virus (AAV) injection—The AAV transfer plasmid pAAV-hSyn1-EGFP-P2A-EGFPf-WPRE-HGHpA was a gift from Dr. Guoping Feng (Addgene # 74513). The AAV PHP.eB was packaged at Hope Center Viral Vector Core of Washington University School of Medicine and diluted to 1.5×10^7 vg/μL with 5% D-sorbitol in PBS. For intraventricular injection, P0/1 pups were anesthetized with hypothermia. 1uL of the diluted AAV was injected into each hemisphere (0.8–1mm away from the middle point between Lambda and bregma, 2mm deep) of the pups. The injected mice were placed onto heat pad for body temperature recovery before returning to dam in the cage. We then perfused the injected mice at P18 and their brains were harvested for histological preparation and immunofluorescence of GFP for spine imaging and analysis.

RNA-seq—Total RNA from 5 sex and litter-matched pairs (2 pairs of male mice and 3 pairs of female mice) of P18 cortical tissues of *Usp7* WT; *Trp53*$^{+/-}$ and *Usp7* cKO; *Trp53*$^{+/-}$ mice was extracted with RNeasy Plus Mini Kit (QIAGEN) for RNA-seq analysis. RNA samples were submitted to the McDonnell Genome Institute at Washington University in St. Louis for RNA-seq library generation and sequencing (Illumina NovoSeq). Total RNA integrity was determined using Agilent Bioanalyzer or 4200 Tapestation. Library preparation was performed with 500ng to 1ug of total RNA. Ribosomal RNA was removed by an RNase-H method using RiboErase kits (Kapa Biosystems). mRNA was then fragmented in reverse transcriptase buffer and heating to 94° for 8 min mRNA was reverse transcribed to yield cDNA using SuperScript III RT enzyme (Life Technologies, per manufacturer's instructions) and random hexamers to ensure complete coverage of gene body. A second strand reaction was performed to yield ds-cDNA. cDNA was blunt ended, had an A base added to the 3′ ends, and then had Illumina sequencing adapters ligated to the ends. Ligated fragments were then amplified for 12–15 cycles using primers incorporating unique dual index tags. Fragments were sequenced with 50 million reads per sample on an Illumina NovaSeq X Plus using paired end reads extending 150 bases. Basecalls and demultiplexing were performed with Illumina's DRAGEN and BCLconvert version 4.2.4 software.

Airyscan imaging and spine analysis—We used Zeiss 880 LSM2 confocal microscope with Airyscan hexagonal detector array and oil immersion to image z-stacks of dendritic spines at near-super resolution. For *in vivo* spine analysis, coronal sections at 100um thickness were float-stained for GFP. Based on Allen mouse reference atlas, motor cortices (M1 and M2) were imaged and 3–8 pyramidal neurons per section, 4 consecutive sections per animal, 3 animals per genotype were analyzed. The analysis was restricted to secondary apical dendritic segment and secondary or tertiary basal dendritic segment, starting from less than 40um distance to soma and for over 30um length. Representative

images of dendritic spines of four shape categories (mushroom, thin, stubby and filopodial) were pre-selected before quantification and used as references to compare with all other dendritic spines to call their shape in a blinded manner. For *in vitro* spine analysis, primary cortical neurons were seeded onto #1.5 coverslips. The neurons were transduced with lentivirus of MISSION TRC1-shRNA (Sigma) knocking down candidate substrates at DIV4, sparsely transfected with EGFP-expressing plasmid at DIV10, fixed at DIV18, and proceeded to immunocytochemistry of GFP and PSD95. Dendritic spines of 4–12 neurons were imaged per well, 3 wells per group, from 2 batches of cortical neuron culture. The analysis was restricted to primary, 2nd and 3rd dendrites starting from less than 40μm distance to soma and for over 30μm length. The spines and PSD95 puncta were counted with Zeiss ZEN software in three dimensional view on a blinded basis. We used Imaris (Oxford Instruments) filament tracing to measure dendrite length in three dimensional view and divide counted number of spines and PSD95 puncta to get spine and PSD95 puncta density, respectively.

Dendrite tracing and morphological analysis—To assess dendrite morphology, primary cortical neurons from *Usp7*$^{fl/fl}$; *Trp53*$^{+/-}$ embryos were seeded onto #1 coverslips and transduced with Cre lentivirus at DIV3. The neurons was sparsely transfected with EGFP-expressing plasmid at DIV9, fixed at DIV11 for immunocytochemistry of GFP. The z-stacks of GFP signal were imaged with Zeiss 880 LSM2 confocal microscope and regular 20x objective. Based on the GFP signal, we used Imaris (Oxford Instruments) to model soma shape and trace dendrite morphology with filament-Autopath algorithm. Physically crossing dendrites were manually separated. Statistics of soma volumes, dendrite lengths and Sholl intersections were all determined and exported with Imaris filament. Complete dendrites of 9–15 neurons per well, 3 wells per group, from 2 batches of neuron culture were imaged and analyzed. All image acquisition and analysis were performed on a blinded basis.

MTS assay—Viability of the primary cortical neurons was assessed according to our previous publication.[75] Briefly, MTS reagent (Promega) was added to neurons 1:5 ratio relative to medium volume at DIV11 according to manufacturer's instructions. The treated neurons were incubated at 37°C with 5% CO_2 for 2 h before measurement of absorbance at 490nm. The measured MTS absorbance was subtracted with background signal in empty wells and normalized to control group (Cre dead or untreated neurons).

QUANTIFICATION AND STATISTICAL ANALYSIS

RNA-seq analysis—For gene-level analysis, RNA-seq reads were aligned to the Ensembl GRCm38.101 primary assembly with STAR version 2.7.9a.[76] Gene counts were derived from the number of uniquely aligned unambiguous reads by Subread:featureCount version 2.0.3.[77] Sequencing performance was assessed for the total number of aligned reads, total number of uniquely aligned reads, and features detected. The ribosomal fraction, known junction saturation, and read distribution over known gene models were quantified with RSeQC version 4.0.[78] All gene counts were then imported into the R/Bioconductor package EdgeR[79] and TMM normalization size factors were calculated to adjust for differences in library size. Ribosomal genes and genes not expressed in at least five samples greater than one count-per-million were excluded from further analysis. The TMM size factors and the

matrix of counts were then imported into the R/Bioconductor package Limma.[80] Weighted likelihoods based on the observed mean-variance relationship of every gene and sample were then calculated for all samples and the count matrix was transformed to moderated log 2 counts-per-million with Limma's voomWithQualityWeights.[81] Differential expression analysis was then performed to analyze for differences between *Usp7* cKO; *Trp53*$^{+/-}$ and Usp7 WT; *Trp53*$^{+/-}$ with blocking factors for litter and sex.

RNA splicing analysis—For differential intron splicing (exon-exon junction) analysis, LeafCutter v0.2.9 was run with default parameters unless otherwise specified, following the protocol described in the prior paper.[34] Briefly, fastq files were aligned to GRCm38 (Ensembl GTF release 102) using the STAR aligner, v2.7.9a, with flag "–outSAMstrandField intronMotif". The resulting BAM files were sorted and indexed using samtools v1.10. Junctions were extracted using regtools v1.0.0, with minimum intron length set to 50. LeafCutter's 'leafcutter_cluster_regtools.py' script was used (with flag "-m 50") to identify intron clusters and quantify junction usage. Finally, differential splicing analysis was run using the 'leafcutter_ds.R′ script from LeafCutter. All results and PCA plots were visualized using LeafCutter's Shiny app.

For differential exon usage analysis, DEXSeq v1.34.1 was used.[35,36] Exon annotation files were produced using the 'dexseq_prepare_annotation.py' script with the "–aggregate no" flag. Fastq files were aligned to GRCm38 (Ensembl GTF release 102) using the STAR aligner, v2.7.9a. Initial count tables were generated using DEXSeq's 'dexseq_count.py' script. All downstream analysis was run with default parameters using DEXSeq's Standard Analysis Workflow. The PCA plot was generated as follows: the exon count matrix was filtered to exclude any exons that did not have at least 10 counts in 3 or more samples. This filtered matrix was 'regularized log'-transformed using the function 'rlog' from DESeq2 v1.44.0. PCA was performed on the rlog-transformed matrix using the 'prcomp' function from the stats package v4.4.0, and the final plot was generated using the 'autoplot' function from ggplot2 v3.5.1.

Gene set enrichment analysis (GSEA)—GSEA 4.3.2[82,83] was used to identify the significantly enrichment of annotated gene sets between proteins in cortices of *Usp7* WT and *Usp7* cKO mice. Gene sets were from M5 (gene ontology) of Molecular signatures database. gene sets with p-value<0.05 with calculated NES values were loaded into Cytoscape 3.9.1 for network construction. The enrichment map was constructed with yfiles Organic Layout, q-value<0.01 as node cutoff, and similarity<0.5 as edge cutoff. All gene sets shown in the enrichment map were enriched in *Usp7* WT mice and associated with down-regulated proteins in *Usp7* cKO mice, as indicated by the green color (color scheme: PiYG-3). Gene sets enriched in *Usp7* cKO mice (associated with up-regulated proteins) were separately visualized with the R package ClusterProfiler.

Gene ontology analysis—For ranked differential protein list, GOrilla[21] (http://cbl-gorilla.cs.technion.ac.il) was used to identify significantly enriched gene ontology terms in ranked gene list. For *in vivo* TMT protein abundance, n = 131 proteins down-regulated in Usp7 cKO mice (Fold Change <0.75) were ranked by Fold Change and loaded to GOrilla with a background of total proteins detected in the TMT experiment. 3 uncharacterized

proteins without gene name were not detected by GOrilla. No GO term was significantly enriched in *Usp7* cKO up-regulated proteins. For differentially spliced gene list in the RNA-seq data, genes with differential exon-exon junction from LeafCutter or differential exon usage from DEXSeq (all FDR<0.05) were selected and analyzed with the package ClusterProfiler in R.

SynGO analysis—For SynGO analysis, unranked down-regulated proteins in *Usp7* cKO; *Trp53*$^{+/-}$ cortex in TMT-MS experiment were identified with a cutoff of Fold Change<0.75 and 2-tail unpaired t test *p*-value<0.01. All proteins detected were used as background. The SynGO enrichment analysis was performed with the SynGO (v1.2) tool for both cellular components and biological processes (https://syngoportal.org).[22]

STRING network analysis—The String network was built with StringApp 2.0.1[24] in Cytoscape 3.9.1. To ensure specificity, we calculated the enrichment percentage of the spectral counts in USP7 TRAF WT group, and only interactors with over 95% enrichment were included for the following analysis. Top 50 interactors based on spectral counts normalized to protein length (Spectrual counts/SeqLen) were converted into homologous mouse proteins and loaded into StringApp to create the association map. Two uncharacterized rat proteins were not included. Full STRING network with edges of confidence over 0.4 was built. Enriched molecular components (Gene ontology) were assigned to subunits of the complex in the association map. FDR of each enriched molecular components was calculated with the Benjamini-Hochberg procedure.

Disease gene enrichment analysis—Interactors of the USP7 TRAF domain used in the disease gene enrichment analysis include only proteins detected in all 3 biological replicates to avoid stochastic bias. The interactors were filtered with 95% enrichment in USP7 TRAF WT group, as described in the String network analysis. All proteins in primary neuron culture detected by TMT-mass spectometry were used as background. Curated pathogenic gene sets for autism, intellectual disability (ID), Epilepsy, ADHD, schizophrenia, bipolar disorder and cerebral palsy were from Geisinger developmental brain disorder gene database (https://dbd.geisingeradmi.org/).[25] High-confidence FMRP targets were from FMRP enriched genes in HITS-CLIP.[26] USP7 TRAF interactors, FMRP targets, and the background proteins were all converted into human orthologs entrez ID with biomaRt R package before the analysis. *p*-values of the disease gene set enrichment were calculated with one-sided hypergeometric test, and then adjusted by Benjamini-Hochberg procedure.

Principal component analysis (PCA)—PCA plots of all proteomics experiments were performed with function prcomp() of R. All detected proteins or genes were loaded into the analysis and principal component 1 and 2 were mapped with variance percentage.

Selection of candidate substrates—To filter out proteins with little to no expression in glutamatergic neurons, we used Allen Institute Smart-Seq dataset[84] to calculate the total CPM of the corresponding gene in the clade of glutamatergic neuron clusters. Proteins with total CPM level in glutamatergic neurons below that of the astrocyte marker aldolase C were excluded from the following analyses. To select candidate substrates of USP7, we first calculated the Euclidean distance of each protein to USP7 over all 16 samples and sorted

out the 25 proteins closest to USP7 as majority of the candidate substrates. Because the sorting based only on Euclidean distance overlooks the proteins with differential abundances between the two time points (DIV6 and DIV8), a 2×2 two-way ANOVA was also applied to all proteins to calculate the *p*-values of Cre and Cre-time interaction effect on the abundance of each protein. Proteins down-regulated upon wild-type Cre expression with *p*-values < 10^{-7} were added to the candidate substrate list.

Weighted gene correlation network analysis (WGCNA)—The R package WGCNA[85] was used to construct a co-expression network for all the proteins with significant Cre effect ($n = 2307$) or Cre-time interaction effect ($n = 320$) ($p < 0.05$ by two-way ANOVA). All 16 TMT samples were used to calculate Pearson correlation matrices representing co-expression similarity of proteins, and different Cre condition (Cre WT and Cre dead) and time points (DIV6 and DIV8) were loaded as traits. The weighted adjacency matrix was created using Pearson correlation coefficient test of all differentially expressed proteins and transformed into a topological overlap measure (TOM) matrix and average linkage hierarchical clustering of the TOM matrix was used to construct a clustering dendrogram of the genes with thresholding power 12. 10 Modules in different colors were generated with minimal gene module size of 30 proteins and minimal height to merge modules of 0.15. GO term enrichment analyses for the modules were performed by DAVID 2021 Functional Annotation Tool[86,87] with a background of all module-assigned proteins. For module-trait relationship, Cre WT, Cre dead, DIV6 and DIV8 were assigned as 1, 0, 6 and 8 respectively. The correlation coefficient and correlation *p*-value of the first principal component of the module gene expression profile (eigengene) and traits were calculated to identify trait-correlated modules.

Statistics—All statistical analyses were performed using IBM SPSS Statistic software (v.26), GraphPad Prism (v.9) and R. For experiments to compare only two groups, student t-test was used. Analysis of variance (ANOVA), (one-way, two-way, factorial, repeated measures) were used analyze data with multiple groups. With a statistically significant interaction between main factors, simple main effects were calculated to provide clarification of statistically significant between-group and within-group differences. Where appropriate, the Huynh-Feldt adjustment was used to protect against violations of sphericity. For multiple pairwise comparisons and post-hoc tests, Tukey correction was applied to compare every two means, and Bonferroni correction was applied to compare selected means when independence cannot be assumed. For three groups with non-normal distributions (sensorimotor battery), the nonparametric Kruskal-Wallis test was used followed by post hoc test with the Dunn correction to compare every mean to a control mean. All data in bar graphs were presented as mean ± SEM and probability value for all analyses was $*p < 0.05$, $**p < 0.01$, $***p < 0.001$, $****p < 0.0001$, unless otherwise stated.

Supplementary Material

Refer to Web version on PubMed Central for supplementary material.

ACKNOWLEDGMENTS

The authors would like to thank the Kim lab and Bonni lab members for critical feedback. The authors also thank A. Yen for help with AAV injection and N. Mosammaparast and N. Tsao for help with the TUBE assay. This work was supported by NIH/NINDS R01NS051255 (to A.B. and A.H.K.), R01 NS111014 (to H.Y.), NIH/NIGMS R01 GM132129 (to J.A.P.), and GM67945 (to S.P.G.); a McDonnell Center for Systems Neuroscience grant (to A.H.K.); the Christopher Davidson and Knight Family Fund (to A.H.K.); and the Duesenberg Research Fund (to A.H.K.). This work was also supported by the Washington University Center for Cellular Imaging (S10 OD21629–01A1-WUCCI) and the Hope Center Viral Vectors Core at Washington University School of Medicine. The graphical abstract was generated using BioRender.

REFERENCES

1. Kishino T, Lalande M, and Wagstaff J (1997). UBE3A/E6-AP mutations cause Angelman syndrome. Nat. Genet. 15, 70–73. 10.1038/ng0197-70. [PubMed: 8988171]
2. Margolin DH, Kousi M, Chan Y-M, Lim ET, Schmahmann JD, Hadjivassiliou M, Hall JE, Adam I, Dwyer A, Plummer L, et al. (2013). Ataxia, dementia, and hypogonadotropism caused by disordered ubiquitination. N. Engl. J. Med. 368, 1992–2003. 10.1056/NEJMoa1215993. [PubMed: 23656588]
3. Alqwaifly M, and Bohlega S (2016). Ataxia and Hypogonadotropic Hypogonadism with Intrafamilial Variability Caused by RNF216 Mutation. Neurol. Int 8, 6444. 10.4081/ni.2016.6444. [PubMed: 27441066]
4. Ferguson CJ, Urso O, Bodrug T, Gassaway BM, Watson ER, Prabu JR, Lara-Gonzalez P, Martinez-Chacin RC, Wu DY, Brigatti KW, et al. (2022). APC7 mediates ubiquitin signaling in constitutive heterochromatin in the developing mammalian brain. Mol. Cell 82, 90–105.e13. 10.1016/j.molcel.2021.11.031. [PubMed: 34942119]
5. Yamada T, Yang Y, and Bonni A (2013). Spatial organization of ubiquitin ligase pathways orchestrates neuronal connectivity. Trends Neurosci. 36, 218–226. 10.1016/j.tins.2012.12.004. [PubMed: 23332798]
6. Anckar J, and Bonni A (2015). Regulation of Neuronal Morphogenesis and Positioning by Ubiquitin-Specific Proteases in the Cerebellum. PLoS One 10, e0117076. 10.1371/journal.pone.0117076. [PubMed: 25607801]
7. Jolly LA, Kumar R, Penzes P, Piper M, and Gecz J (2022). The DUB Club: Deubiquitinating Enzymes and Neurodevelopmental Disorders. Biol. Psychiatry 92, 614–625. 10.1016/j.biopsych.2022.03.022. [PubMed: 35662507]
8. Hao Y-H, Fountain MD Jr., Fon Tacer K, Xia F, Bi W, Kang SHL, Patel A, Rosenfeld JA, Le Caignec C, Isidor B, et al. (2015). USP7 Acts as a Molecular Rheostat to Promote WASH-Dependent Endosomal Protein Recycling and Is Mutated in a Human Neurodevelopmental Disorder. Mol. Cell 59, 956–969. 10.1016/j.molcel.2015.07.033. [PubMed: 26365382]
9. Fountain MD, Oleson DS, Rech ME, Segebrecht L, Hunter JV, McCarthy JM, Lupo PJ, Holtgrewe M, Moran R, Rosenfeld JA, et al. (2019). Pathogenic variants in USP7 cause a neurodevelopmental disorder with speech delays, altered behavior, and neurologic anomalies. Genet. Med. 21, 1797–1807. 10.1038/s41436-019-0433-1. [PubMed: 30679821]
10. Cummins JM, Rago C, Kohli M, Kinzler KW, Lengauer C, and Vogelstein B (2004). Tumour suppression: disruption of HAUSP gene stabilizes p53. Nature 428, 1–486. 10.1038/nature02501.
11. Li M, Brooks CL, Kon N, and Gu W (2004). A Dynamic Role of HAUSP in the p53-Mdm2 Pathway. Mol. Cell 13, 879–886. 10.1016/S1097-2765(04)00157-1. [PubMed: 15053880]
12. Turnbull AP, Ioannidis S, Krajewski WW, Pinto-Fernandez A, Heride C, Martin ACL, Tonkin LM, Townsend EC, Buker SM, Lancia DR, et al. (2017). Molecular basis of USP7 inhibition by selective small-molecule inhibitors. Nature 550, 481–486. 10.1038/nature24451. [PubMed: 29045389]
13. Kategaya L, Di Lello P, Rougé L, Pastor R, Clark KR, Drummond J, Kleinheinz T, Lin E, Upton JP, Prakash S, et al. (2017). USP7 Small-Molecule Inhibitors Interfere with Ubiquitin Binding (Nature Publishing Group). 10.1038/nature24006.

14. Kon N, Kobayashi Y, Li M, Brooks CL, Ludwig T, and Gu W (2010). Inactivation of HAUSP in vivo modulates p53 function. Oncogene 29, 1270–1279. 10.1038/onc.2009.427. [PubMed: 19946331]

15. Kon N, Zhong J, Kobayashi Y, Li M, Szabolcs M, Ludwig T, Canoll PD, and Gu W (2011). Roles of HAUSP-mediated p53 regulation in central nervous system development. Cell Death Differ. 18, 1366–1375. 10.1038/cdd.2011.12. [PubMed: 21350561]

16. Huang Z, Wu Q, Guryanova OA, Cheng L, Shou W, Rich JN, and Bao S (2011). Deubiquitylase HAUSP stabilizes REST and promotes maintenance of neural progenitor cells. Nat. Cell Biol. 13, 142–152. 10.1038/ncb2153. [PubMed: 21258371]

17. Nicklas S, Hillje AL, Okawa S, Rudolph IM, Collmann FM, van Wuellen T, del Sol A, and Schwamborn JC (2019). A complex of the ubiquitin ligase TRIM32 and the deubiquitinase USP7 balances the level of c-Myc ubiquitination and thereby determines neural stem cell fate specification. Cell Death Differ. 26, 728–740. 10.1038/s41418-018-0144-1. [PubMed: 29899379]

18. Kim RQ, and Sixma TK (2017). Regulation of USP7: A High Incidence of E3 Complexes. J. Mol. Biol. 429, 3395–3408. 10.1016/J.JMB.2017.05.028. [PubMed: 28591556]

19. Goebbels S, Bormuth I, Bode U, Hermanson O, Schwab MH, and Nave K-A (2006). Genetic targeting of principal neurons in neocortex and hippocampus of NEX-Cre mice. Genesis 44, 611–621. 10.1002/dvg.20256. [PubMed: 17146780]

20. Hashikawa K, Hashikawa Y, Lischinsky J, and Lin D (2018). The Neural Mechanisms of Sexually Dimorphic Aggressive Behaviors. Trends Genet. 34, 755–776. 10.1016/j.tig.2018.07.001. [PubMed: 30173869]

21. Eden E, Navon R, Steinfeld I, Lipson D, and Yakhini Z (2009). GOrilla: A tool for discovery and visualization of enriched GO terms in ranked gene lists. BMC Bioinf. 10, 48–57. 10.1186/1471-2105-10-48.

22. Koopmans F, van Nierop P, Andres-Alonso M, Byrnes A, Cijsouw T, Coba MP, Cornelisse LN, Farrell RJ, Goldschmidt HL, Howrigan DP, et al. (2019). SynGO: An Evidence-Based, Expert-Curated Knowledge Base for the Synapse. Neuron 103, 217–234.e4. 10.1016/J.NEURON.2019.05.002. [PubMed: 31171447]

23. Sheng Y, Saridakis V, Sarkari F, Duan S, Wu T, Arrowsmith CH, and Frappier L (2006). Molecular recognition of p53 and MDM2 by USP7/HAUSP. Nat. Struct. Mol. Biol. 13, 285–291. 10.1038/nsmb1067. [PubMed: 16474402]

24. Szklarczyk D, Franceschini A, Wyder S, Forslund K, Heller D, Huerta-Cepas J, Simonovic M, Roth A, Santos A, Tsafou KP, et al. (2015). STRING v10: protein–protein interaction networks, integrated over the tree of life. Nucleic Acids Res. 43, D447–D452. 10.1093/nar/gku1003. [PubMed: 25352553]

25. Gonzalez-Mantilla AJ, Moreno-De-Luca A, Ledbetter DH, and Martin CL (2016). A cross-disorder method to identify novel candidate genes for developmental brain disorders. JAMA Psychiatr. 73, 275–283. 10.1001/jamapsychiatry.2015.2692.

26. Darnell JC, Van Driesche SJ, Zhang C, Hung KYS, Mele A, Fraser CE, Stone EF, Chen C, Fak JJ, Chi SW, et al. (2011). FMRP stalls ribosomal translocation on mRNAs linked to synaptic function and autism. Cell 146, 247–261. 10.1016/j.cell.2011.06.013. [PubMed: 21784246]

27. Chahrour MH, Yu TW, Lim ET, Ataman B, Coulter ME, Hill RS, Stevens CR, Schubert CR, and ARRA Autism Sequencing Collaboration; and Greenberg, M.E. (2012). Whole-Exome Sequencing and Homozygosity Analysis Implicate Depolarization-Regulated Neuronal Genes in Autism. PLoS Genet. 8, e1002635. [PubMed: 22511880]

28. Zhang J, Gambin T, Yuan B, Szafranski P, Rosenfeld JA, Balwi MA, Alswaid A, Al-Gazali L, Shamsi AMA, Komara M, et al. (2017). Haploinsufficiency of the E3 ubiquitin-protein ligase gene TRIP12 causes intellectual disability with or without autism spectrum disorders, speech delay, and dysmorphic features. Hum. Genet. 136, 377–386. 10.1007/s00439-017-1763-1. [PubMed: 28251352]

29. Hjerpe R, Aillet F, Lopitz-Otsoa F, Lang V, England P, and Rodriguez MS (2009). Efficient protection and isolation of ubiquitylated proteins using tandem ubiquitin-binding entities. EMBO Rep. 10, 1250–1258. 10.1038/embor.2009.192. [PubMed: 19798103]

30. Lelieveld SH, Reijnders MRF, Pfundt R, Yntema HG, Kamsteeg E-J, de Vries P, de Vries BBA, Willemsen MH, Kleefstra T, Löhner K, et al. (2016). Meta-analysis of 2,104 trios provides support for 10 new genes for intellectual disability. Nat. Neurosci. 19, 1194–1196. 10.1038/nn.4352. [PubMed: 27479843]

31. Vissers LELM, Van Nimwegen KJM, Schieving JH, Kamsteeg EJ, Kleefstra T, Yntema HG, Pfundt R, Van Der Wilt GJ, Krabbenborg L, Brunner HG, et al. (2017). A clinical utility study of exome sequencing versus conventional genetic testing in pediatric neurology. Genet. Med. 19, 1055–1063. 10.1038/GIM.2017.1. [PubMed: 28333917]

32. Iossifov I, O'Roak BJ, Sanders SJ, Ronemus M, Krumm N, Levy D, Stessman HA, Witherspoon KT, Vives L, Patterson KE, et al. (2014). The contribution of de novo coding mutations to autism spectrum disorder. Nature 515, 216–221. 10.1038/nature13908. [PubMed: 25363768]

33. De Rubeis S, He X, Goldberg AP, Poultney CS, Samocha K, Cicek AE, Kou Y, Liu L, Fromer M, Walker S, et al. (2014). Synaptic, transcriptional and chromatin genes disrupted in autism. Nature 515, 209–215. 10.1038/nature13772. [PubMed: 25363760]

34. Li YI, Knowles DA, Humphrey J, Barbeira AN, Dickinson SP, Im HK, and Pritchard JK (2018). Annotation-free quantification of RNA splicing using LeafCutter. Nat. Genet. 50, 151–158. 10.1038/s41588-017-0004-9. [PubMed: 29229983]

35. Anders S, Reyes A, and Huber W (2012). Detecting differential usage of exons from RNA-seq data. Genome Res. 22, 2008–2017. 10.1101/gr.133744.111. [PubMed: 22722343]

36. Reyes A, Anders S, Weatheritt RJ, Gibson TJ, Steinmetz LM, and Huber W (2013). Drift and conservation of differential exon usage across tissues in primate species. Proc. Natl. Acad. Sci. USA 110, 15377–15382. 10.1073/pnas.1307202110. [PubMed: 24003148]

37. Garcia EP, McPherson PS, Chilcote TJ, Takei K, and De Camilli P (1995). rbSec1A and B colocalize with syntaxin 1 and SNAP-25 throughout the axon, but are not in a stable complex with syntaxin. J. Cell Biol. 129, 105–120. 10.1083/jcb.129.1.105. [PubMed: 7698978]

38. Meijer M, Cijsouw T, Toonen RF, and Verhage M (2015). Synaptic Effects of Munc18–1 Alternative Splicing in Excitatory Hippocampal Neurons. PLoS One 10, e0138950. [PubMed: 26407320]

39. Ramos-Miguel A, Hercher C, Beasley CL, Barr AM, Bayer TA, Falkai P, Leurgans SE, Schneider JA, Bennett DA, and Honer WG (2015). Loss of Munc18–1 long splice variant in GABAergic terminals is associated with cognitive decline and increased risk of dementia in a community sample. Mol. Neurodegener. 10, 65. 10.1186/s13024-015-0061-4. [PubMed: 26628003]

40. Penzes P, Johnson RC, Alam MR, Kambampati V, Mains RE, and Eipper BA (2000). An Isoform of Kalirin, a Brain-specific GDP/GTP Exchange Factor, Is Enriched in the Postsynaptic Density Fraction. J. Biol. Chem. 275, 6395–6403. 10.1074/jbc.275.9.6395. [PubMed: 10692441]

41. Penzes P, Johnson RC, Sattler R, Zhang X, Huganir RL, Kambampati V, Mains RE, and Eipper BA (2001). The Neuronal Rho-GEF Kalirin-7 Interacts with PDZ Domain-Containing Proteins and Regulates Dendritic Morphogenesis. Neuron 29, 229–242. 10.1016/S0896-6273(01)00193-3. [PubMed: 11182094]

42. Penzes P, and Jones KA (2008). Dendritic spine dynamics-a key role for kalirin-7. Trends Neurosci. 31, 419–427. 10.1016/j.tins.2008.06.001. [PubMed: 18597863]

43. Schwab ME (2010). Functions of Nogo proteins and their receptors in the nervous system. Nat. Rev. Neurosci. 11, 799–811. 10.1038/nrn2936. [PubMed: 21045861]

44. Tavana O, and Gu W (2017). Modulation of the p53/MDM2 interplay by HAUSP inhibitors. J. Mol. Cell Biol. 9, 45–52. 10.1093/jmcb/mjw049.

45. Schmitzová J, Cretu C, Dienemann C, Urlaub H, and Pena V (2023). Structural basis of catalytic activation in human splicing. Nature 617, 842–850. 10.1038/s41586-023-06049-w. [PubMed: 37165190]

46. Zhang X, Lu Y, and Shi Y (2024). Molecular basis for the activation of human spliceosome. Nat. Commun. 15, 6348. 10.1038/s41467-024-50785-0. [PubMed: 39068178]

47. Vuong CK, Black DL, and Zheng S (2016). The neurogenetics of alternative splicing. Nat. Rev. Neurosci. 17, 265–281. 10.1038/nrn.2016.27. [PubMed: 27094079]

48. Furlanis E, Traunmüller L, Fucile G, and Scheiffele P (2019). Landscape of ribosome-engaged transcript isoforms reveals extensive neuronal-cell-class-specific alternative splicing programs. Nat. Neurosci. 22, 1709–1717. 10.1038/s41593-019-0465-5. [PubMed: 31451803]
49. Ule J, Ule A, Spencer J, Williams A, Hu J-S, Cline M, Wang H, Clark T, Fraser C, Ruggiu M, et al. (2005). Nova regulates brain-specific splicing to shape the synapse. Nat. Genet. 37, 844–852. 10.1038/ng1610. [PubMed: 16041372]
50. Zoghbi HY, and Bear MF (2012). Synaptic dysfunction in neurodevelopmental disorders associated with autism and intellectual disabilities. Cold Spring Harb. Perspect. Biol. 4, a009886. 10.1101/cshperspect.a009886. [PubMed: 22258914]
51. Volk L, Chiu SL, Sharma K, and Huganir RL (2015). Glutamate Synapses in Human Cognitive Disorders. Annu. Rev. Neurosci. 38, 127–149. 10.1146/annurev-neuro-071714-033821. [PubMed: 25897873]
52. Bagni C, and Zukin RS (2019). A Synaptic Perspective of Fragile X Syndrome and Autism Spectrum Disorders. Neuron 101, 1070–1088. 10.1016/J.NEURON.2019.02.041. [PubMed: 30897358]
53. Haakonsen DL, Heider M, Ingersoll AJ, Vodehnal K, Witus SR, Uenaka T, Wernig M, and Rapé M (2024). Stress response silencing by an E3 ligase mutated in neurodegeneration. Nature 626, 874–880. 10.1038/s41586-023-06985-7. [PubMed: 38297121]
54. Shim T, Kim JY, Kim W, Lee Y-I, Cho B, and Moon C (2024). Cullin-RING E3 ubiquitin ligase 4 regulates neurite morphogenesis during neurodevelopment. iScience 27, 108933. 10.1016/j.isci.2024.108933. [PubMed: 38318354]
55. Nuber U, Schwarz SE, and Scheffner M (1998). The ubiquitin-protein ligase E6-associated protein (E6-AP) serves as its own substrate. Eur. J. Biochem. 254, 643–649. 10.1046/j.1432-1327.1998.2540643.x. [PubMed: 9688277]
56. De Bie P, and Ciechanover A (2011). Ubiquitination of E3 ligases: Self-regulation of the ubiquitin system via proteolytic and non-proteolytic mechanisms. Cell Death Differ. 18, 1393–1402. 10.1038/cdd.2011.16. [PubMed: 21372847]
57. Froyen G, Corbett M, Vandewalle J, Jarvela I, Lawrence O, Meldrum C, Bauters M, Govaerts K, Vandeleur L, Van Esch H, et al. (2008). Submicroscopic Duplications of the Hydroxysteroid Dehydrogenase HSD17B10 and the E3 Ubiquitin Ligase HUWE1 Are Associated with Mental Retardation. Am. J. Hum. Genet. 82, 432–443. 10.1016/j.ajhg.2007.11.002. [PubMed: 18252223]
58. Moortgat S, Berland S, Aukrust I, Maystadt I, Baker L, Benoit V, Caro-Llopis A, Cooper NS, Debray FG, Faivre L, et al. (2018). HUWE1 variants cause dominant X-linked intellectual disability: A clinical study of 21 patients. Eur. J. Hum. Genet. 26, 64–74. 10.1038/s41431-017-0038-6. [PubMed: 29180823]
59. Zhang Y, Wolf GW, Bhat K, Jin A, Allio T, Burkhart WA, and Xiong Y (2003). Ribosomal protein L11 negatively regulates oncoprotein MDM2 and mediates a p53-dependent ribosomal-stress checkpoint pathway. Mol. Cell Biol. 23, 8902–8912. 10.1128/MCB.23.23.8902-8912.2003. [PubMed: 14612427]
60. Zhang Q, Gao X, Li C, Feliciano C, Wang D, Zhou D, Mei Y, Monteiro P, Anand M, Itohara S, et al. (2016). Impaired Dendritic Development and Memory in Sorbs2 Knock-Out Mice. J. Neurosci. 36, 2247–2260. 10.1523/JNEUROSCI.2528-15.2016. [PubMed: 26888934]
61. An L, Jiang Y, Ng HHW, Man EPS, Chen J, Khoo U-S, Gong Q, and Huen MSY (2017). Dual-utility NLS drives RNF169-dependent DNA damage responses. Proc. Natl. Acad. Sci. 114, E2872–E2881. 10.1073/pnas.1616602114. [PubMed: 28325877]
62. Spiegel I, Mardinly AR, Gabel HW, Bazinet JE, Couch CH, Tzeng CP, Harmin DA, and Greenberg ME (2014). Npas4 Regulates Excitatory-Inhibitory Balance within Neural Circuits through Cell-Type-Specific Gene Programs. Cell 157, 1216–1229. 10.1016/J.CELL.2014.03.058. [PubMed: 24855953]
63. Prusky GT, Alam NM, Beekman S, and Douglas RM (2004). Rapid quantification of adult and developing mouse spatial vision using a virtual optomotor system. Invest. Ophthalmol. Vis. Sci. 45, 4611–4616. 10.1167/iovs.04-0541. [PubMed: 15557474]

64. Wozniak DF, Diggs-Andrews KA, Conyers S, Yuede CM, Dearborn JT, Brown JA, Tokuda K, Izumi Y, Zorumski CF, and Gutmann DH (2013). Motivational Disturbances and Effects of L-dopa Administration in Neurofibromatosis-1 Model Mice. PLoS One 8, e66024. [PubMed: 23762458]

65. Konishi Y, Lehtinen M, Donovan N, and Bonni A (2002). Cdc2 Phosphorylation of BAD Links the Cell Cycle to the Cell Death Machinery. Mol. Cell 9, 1005–1016. 10.1016/S1097-2765(02)00524-5. [PubMed: 12049737]

66. Elias JE, and Gygi SP (2007). Target-decoy search strategy for increased confidence in large-scale protein identifications by mass spectrometry. Nat. Methods 4, 207–214. 10.1038/nmeth1019. [PubMed: 17327847]

67. Elias JE, and Gygi SP (2010). Target-decoy search strategy for mass spectrometry-based proteomics. Methods Mol. Biol. 604, 55–71. 10.1007/978-1-60761-444-9_5. [PubMed: 20013364]

68. Huttlin EL, Jedrychowski MP, Elias JE, Goswami T, Rad R, Beausoleil SA, Villén J, Haas W, Sowa ME, and Gygi SP (2010). A Tissue-Specific Atlas of Mouse Protein Phosphorylation and Expression. Cell 143, 1174–1189. 10.1016/J.CELL.2010.12.001. [PubMed: 21183079]

69. Navarrete-Perea J, Yu Q, Gygi SP, and Paulo JA (2018). Streamlined Tandem Mass Tag (SL-TMT) Protocol: An Efficient Strategy for Quantitative (Phospho) proteome Profiling Using Tandem Mass Tag-Synchronous Precursor Selection-MS3. J. Proteome Res. 17, 2226–2236. 10.1021/acs.jproteome.8b00217. [PubMed: 29734811]

70. Tsao N, Brickner JR, Rodell R, Ganguly A, Wood M, Oyeniran C, Ahmad T, Sun H, Bacolla A, Zhang L, et al. (2021). Aberrant RNA methylation triggers recruitment of an alkylation repair complex. Mol. Cell 81, 4228–4242.e8. 10.1016/j.molcel.2021.09.024. [PubMed: 34686315]

71. Wang Y, Wang Q, Haldar JP, Yeh F-C, Xie M, Sun P, Tu T-W, Trinkaus K, Klein RS, Cross AH, and Song SK (2011). Quantification of increased cellularity during inflammatory demyelination. Brain 134, 3590–3601. 10.1093/brain/awr307. [PubMed: 22171354]

72. Lin TH, Zhan J, Song C, Wallendorf M, Sun P, Niu X, Yang R, Cross AH, and Song SK (2020). Diffusion Basis Spectrum Imaging Detects Axonal Loss After Transient Dexamethasone Treatment in Optic Neuritis Mice. Front. Neurosci. 14, 592063–592112. 10.3389/fnins.2020.592063. [PubMed: 33551721]

73. Zhan J, Lin TH, Libbey JE, Sun P, Ye Z, Song C, Wallendorf M, Gong H, Fujinami RS, and Song SK (2018). Diffusion basis spectrum and diffusion tensor imaging detect hippocampal inflammation and dendritic injury in a virus-induced mouse model of epilepsy. Front. Neurosci. 12, 77–79. 10.3389/fnins.2018.00077. [PubMed: 29497358]

74. Yushkevich PA, Piven J, Hazlett HC, Smith RG, Ho S, Gee JC, and Gerig G (2006). User-guided 3D active contour segmentation of anatomical structures: Significantly improved efficiency and reliability. Neuroimage 31, 1116–1128. 10.1016/J.NEUROIMAGE.2006.01.015. [PubMed: 16545965]

75. Mao DD, Gujar AD, Mahlokozera T, Chen I, Pan Y, Luo J, Brost T, Thompson EA, Turski A, Leuthardt EC, et al. (2015). A CDC20-APC/SOX2 Signaling Axis Regulates Human Glioblastoma Stem-like Cells. Cell Rep. 11, 1809–1821. 10.1016/J.CELREP.2015.05.027. [PubMed: 26074073]

76. Dobin A, Davis CA, Schlesinger F, Drenkow J, Zaleski C, Jha S, Batut P, Chaisson M, and Gingeras TR (2013). STAR: ultrafast universal RNA-seq aligner. Bioinformatics 29, 15–21. 10.1093/bioinformatics/bts635. [PubMed: 23104886]

77. Liao Y, Smyth GK, and Shi W (2014). featureCounts: an efficient general purpose program for assigning sequence reads to genomic features. Bioinformatics 30, 923–930. 10.1093/bioinformatics/btt656. [PubMed: 24227677]

78. Wang L, Wang S, and Li W (2012). RSeQC: quality control of RNA-seq experiments. Bioinformatics 28, 2184–2185. 10.1093/bioinformatics/bts356. [PubMed: 22743226]

79. Robinson MD, McCarthy DJ, and Smyth GK (2010). edgeR: a Bioconductor package for differential expression analysis of digital gene expression data. Bioinformatics 26, 139–140. 10.1093/bioinformatics/btp616. [PubMed: 19910308]

80. Ritchie ME, Phipson B, Wu D, Hu Y, Law CW, Shi W, and Smyth GK (2015). limma powers differential expression analyses for RNA-sequencing and microarray studies. Nucleic Acids Res. 43, e47. 10.1093/nar/gkv007. [PubMed: 25605792]

81. Liu R, Holik AZ, Su S, Jansz N, Chen K, Leong HS, Blewitt ME, Asselin-Labat M-L, Smyth GK, and Ritchie ME (2015). Why weight? Modelling sample and observational level variability improves power in RNA-seq analyses. Nucleic Acids Res. 43, e97. 10.1093/nar/gkv412. [PubMed: 25925576]

82. Daly MJ, Patterson N, Mesirov JP, Golub TR, Tamayo P, and Spiegelman B (2003). PGC-1a-responsive genes involved in oxidative phosphorylation are coordinately downregulated in human diabetes. Nat. Genet. 34, 267–273. [PubMed: 12808457]

83. Subramanian A, Tamayo P, Mootha VK, Mukherjee S, Ebert BL, Gillette MA, Paulovich A, Pomeroy SL, Golub TR, Lander ES, and Mesirov JP (2005). Gene set enrichment analysis: A knowledge-based approach for interpreting genome-wide expression profiles. Proc. Natl. Acad. Sci. USA 102, 15545–15550. 10.1073/pnas.0506580102. [PubMed: 16199517]

84. Tasic B, Yao Z, Graybuck LT, Smith KA, Nguyen TN, Bertagnolli D, Goldy J, Garren E, Economo MN, Viswanathan S, et al. (2018). Shared and distinct transcriptomic cell types across neocortical areas. Nature 563, 72–78. 10.1038/s41586-018-0654-5. [PubMed: 30382198]

85. Langfelder P, and Horvath S (2008). WGCNA: an R package for weighted correlation network analysis. BMC Bioinf. 9, 559. 10.1186/1471-2105-9-559.

86. Huang DW, Sherman BT, and Lempicki RA (2009). Systematic and integrative analysis of large gene lists using DAVID bioinformatics resources. Nat. Protoc. 4, 44–57. 10.1038/nprot.2008.211. [PubMed: 19131956]

87. Sherman BT, Hao M, Qiu J, Jiao X, Baseler MW, Lane HC, Imamichi T, and Chang W (2022). DAVID: a web server for functional enrichment analysis and functional annotation of gene lists (2021 update). Nucleic Acids Res. 50, W216–W221. 10.1093/nar/gkac194. [PubMed: 35325185]

Highlights

- USP7 deletion in glutamatergic neurons causes disease-relevant behavioral deficits
- USP7 deletion in glutamatergic neurons triggers p53-dependent apoptosis
- USP7 deubiquitinates the RNA splicing factor Ppil4 to regulate synapse development
- USP7 regulates RNA splicing program of synaptic genes in the cerebral cortex

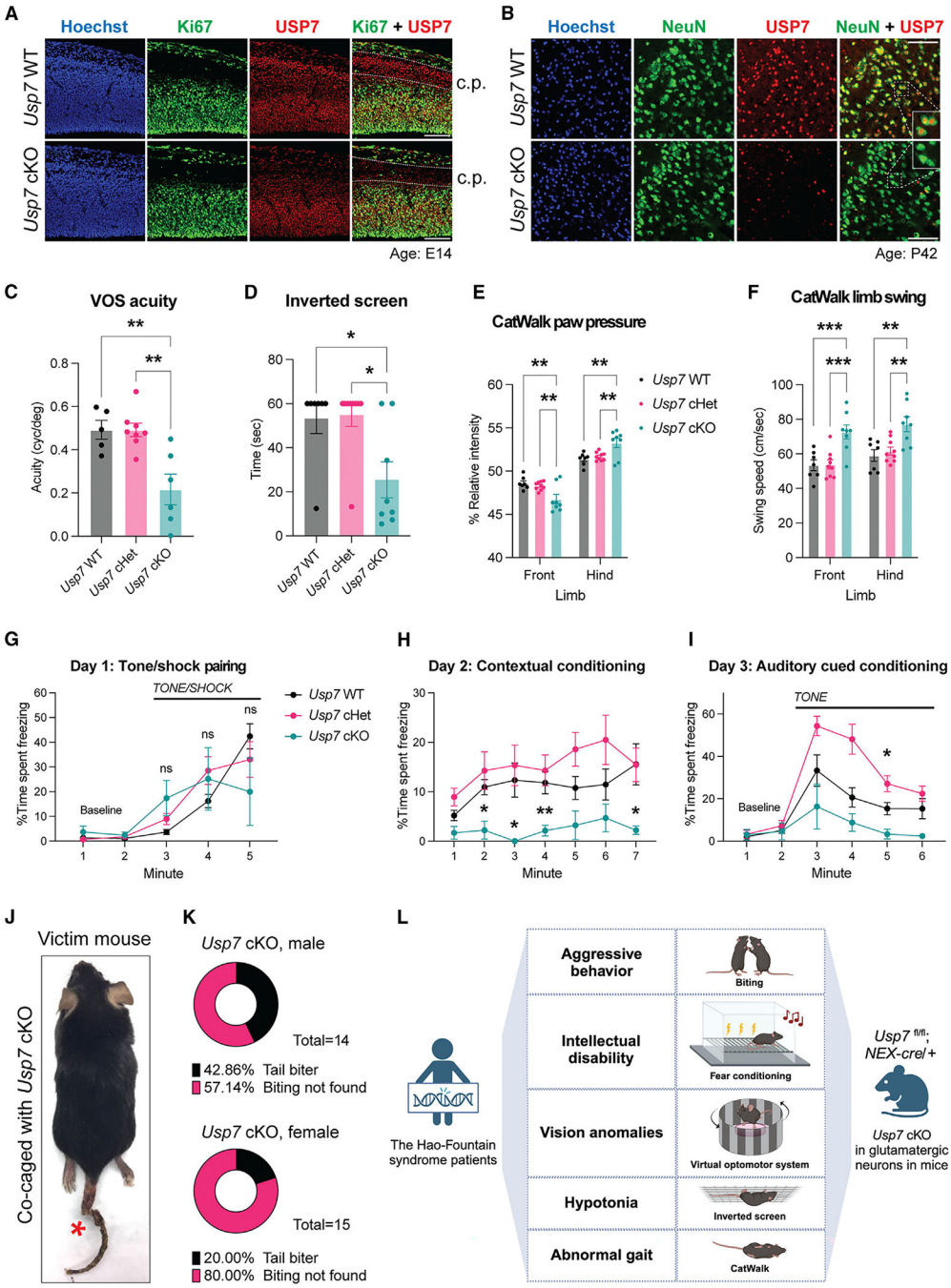

Figure 1. USP7 deletion in glutamatergic neurons causes disease-relevant behavioral deficits in mice

(A and B) Immunofluorescence of USP7 in the cerebral cortex on embryonic day 14 (E14; A) and post-natal day 42 (P42; B). Dashed lines demarcate the cortical plate (c.p.). Scale bars, 100 μm.

(C) Virtual optomotor system (VOS) test: spatial frequency threshold. $^{**}p < 0.01$ by Bonferroni's multiple-comparisons test.

(D) Motor strength test: time to grip onto the inverted screen. $^{*}p < 0.05$ by Dunn's multiple-comparisons test.

(E and F) CatWalk: relative mean intensity distributed onto front- and hindpaws (E) and limb swing speed (F). $^{**}p < 0.01$, $^{***}p < 0.001$ by Tukey's multiple-comparisons test. See also Video S2.

(G–I) Fear conditioning: percentage of freezing time in tone/shock pairing (G), contextual conditioning (H), and auditory cued conditioning (I). $^{*}p < 0.05$, $^{**}p < 0.01$ by Bonferroni's multiple-comparisons test (*Usp7* WT vs. cKO).

(J) Representative biting injury on mice co-caged with *Usp7* cKO mice. See also Video S3.

(K) Percentage of tail biters among *Usp7* cKO mice from 3 to 12 weeks old.

(L) Schematic of behavioral phenotypes in *Usp7* cKO mice that are relevant to HAFOUS.

Data are presented as mean ± SEM. See also Figure S1.

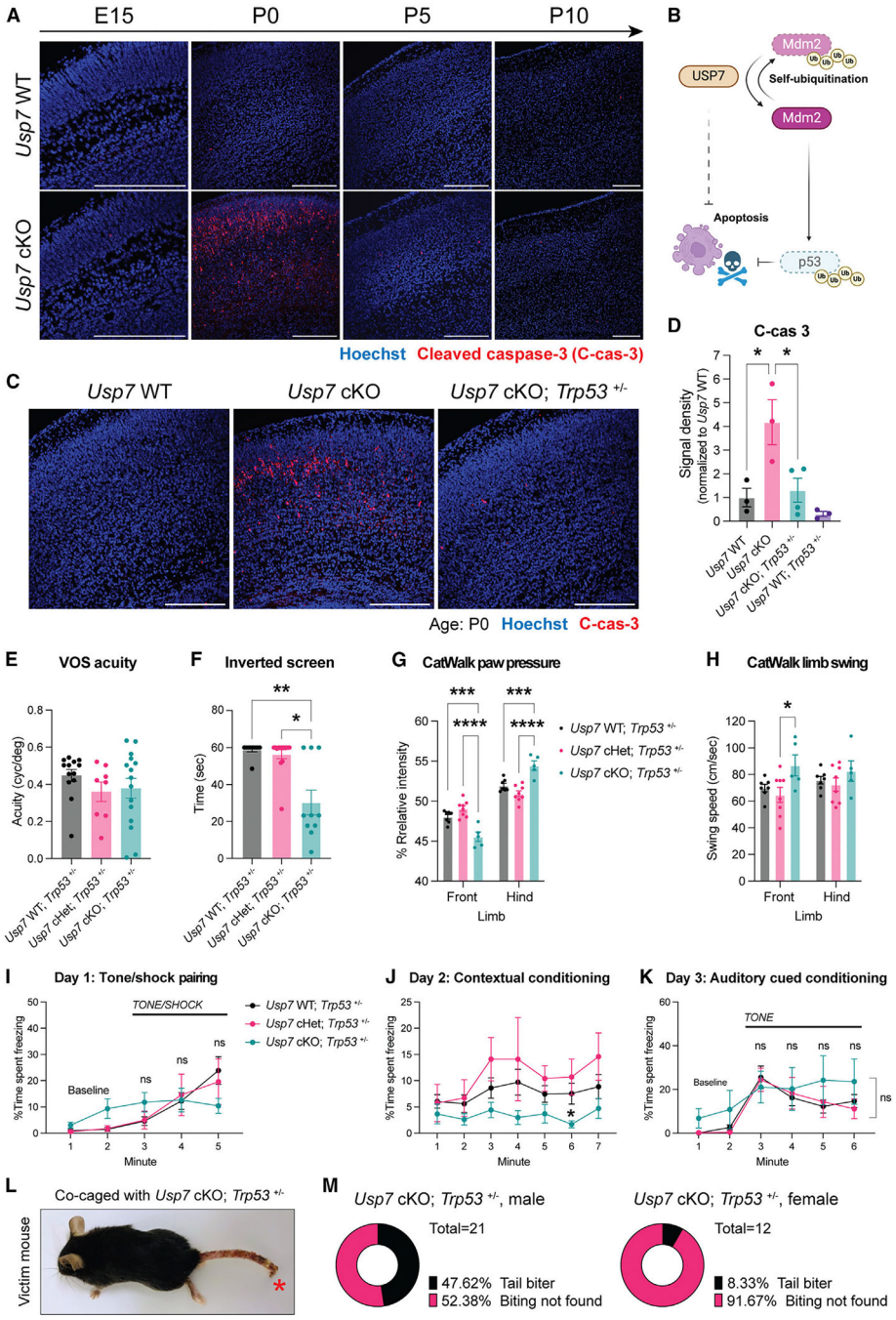

Figure 2. p53 co-deletion rescues apoptosis, impaired visual acuity, and auditory cued conditioning in *Usp7* cKO mice but no other behavioral deficits

(A) Immunofluorescence of c-cas-3 in the cerebral cortex at different ages. Scale bar, 200 μm.

(B) Schematic of the USP7-Mdm2-p53 signaling pathway regulating apoptosis.

(C) Immunofluorescence of c-cas-3 in the cerebral cortex of mice of different *Trp53* and *Usp7* genotypes at P0. Scale bar, 200 μm.

(D) Quantification of c-cas-3 fluorescent signal as in (C). *$p < 0.05$ by Tukey's multiple-comparisons test.

(E) VOS test: spatial frequency threshold. No significant genotype effect by one-way ANOVA.
(F) Motor strength test: time to grip onto the inverted screen. *$p < 0.05$, **$p < 0.01$ by Dunn's multiple-comparisons test.
(G and H) CatWalk: relative mean intensity distributed onto front- and hindpaws (G) and limb swing speed (H). *$p < 0.05$, ***$p < 0.001$, ****$p < 0.0001$ by Tukey's multiple-comparison test. See also Video S4.
(I–K) Fear conditioning: percentage of freezing time in tone/shock pairing (I), contextual conditioning (J), and auditory cued conditioning (K). *$p < 0.05$ by Bonferroni's multiple-comparisons test (*Usp7* WT vs. cKO).
(L) Representative biting injury on mice co-caged with *Usp7* cKO; *Trp53*$^{+/-}$ mice.
(M) Percentage of tail biters among *Usp7* cKO; *Trp53*$^{+/-}$ mice from 3 to 12 weeks old. Data are presented as mean ± SEM. See also Figures S2 and S3.

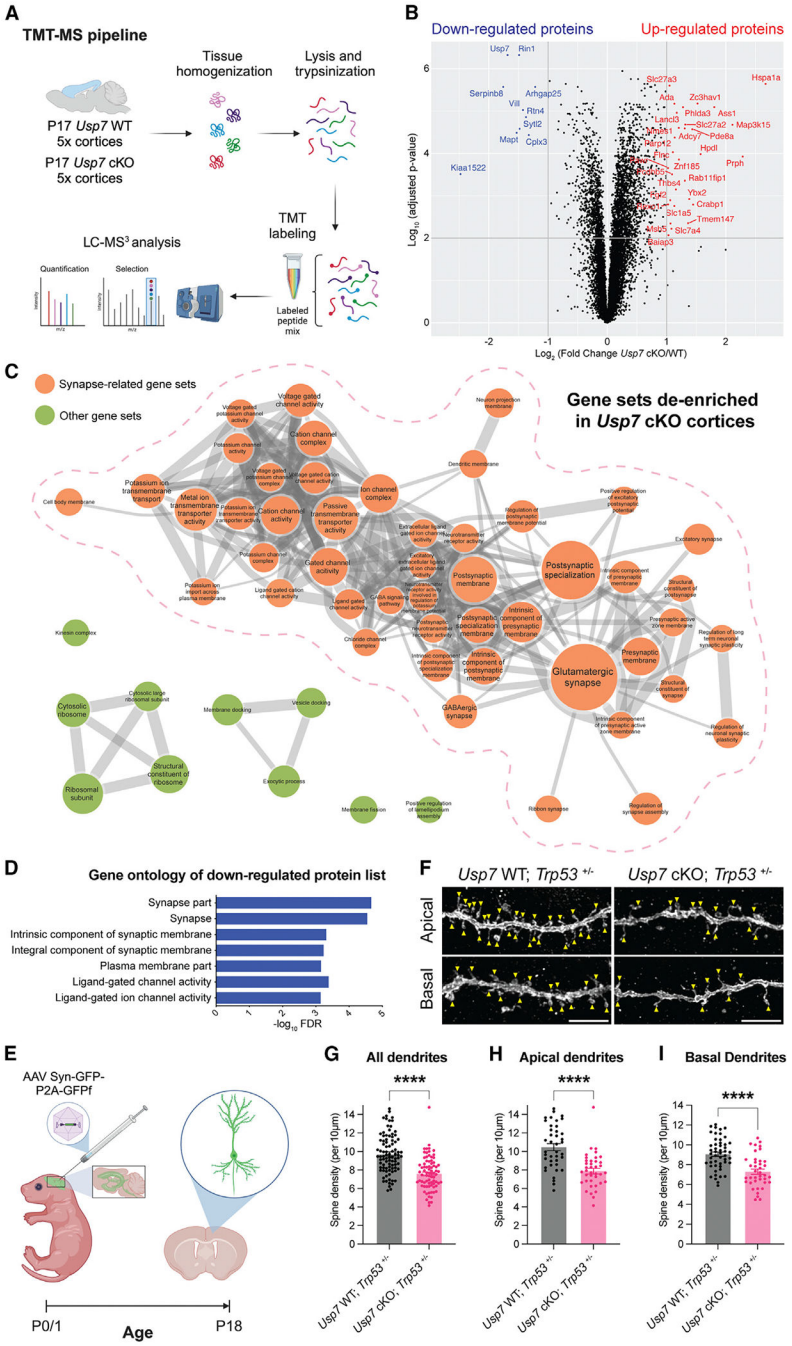

Figure 3. USP7 loss reduces synapses in the cerebral cortex

(A) Flowchart to characterize the proteome of the cerebral cortex with 10-plex TMT-MS.

(B) Volcano plot showing differentially expressed proteins in TMT-MS. The *p* values were calculated by 2-tailed unpaired t test with Benjamini–Hochberg correction.

(C) Network of GO gene sets de-enriched in *Usp7* cKO cortices based on TMT protein abundance. Nodes represent gene sets ($q < 0.01$), and size of nodes represents number of genes. Edges represent GO-defined relations (similarity > 0.5), and thickness of edges

represents similarity between gene sets. Interconnected synapse-related gene sets are circled and colored in orange.

(D) GO terms enriched from downregulated proteins (*Usp7* cKO/WT fold change < 0.75).

(E) Schematic of *in vivo* dendritic spine analysis of cortical pyramidal neurons.

(F) Representative GFP micrographs of dendritic spines (arrowheads) on apical and basal dendrites. Scale bar, 5 μm.

(G–I) Spine density on apical, basal, and all dendrites of pyramidal neurons in the motor cortex. ****$p < 0.0001$ by 2-tailed unpaired t test.

Data are presented as mean ± SEM. See also Figure S4.

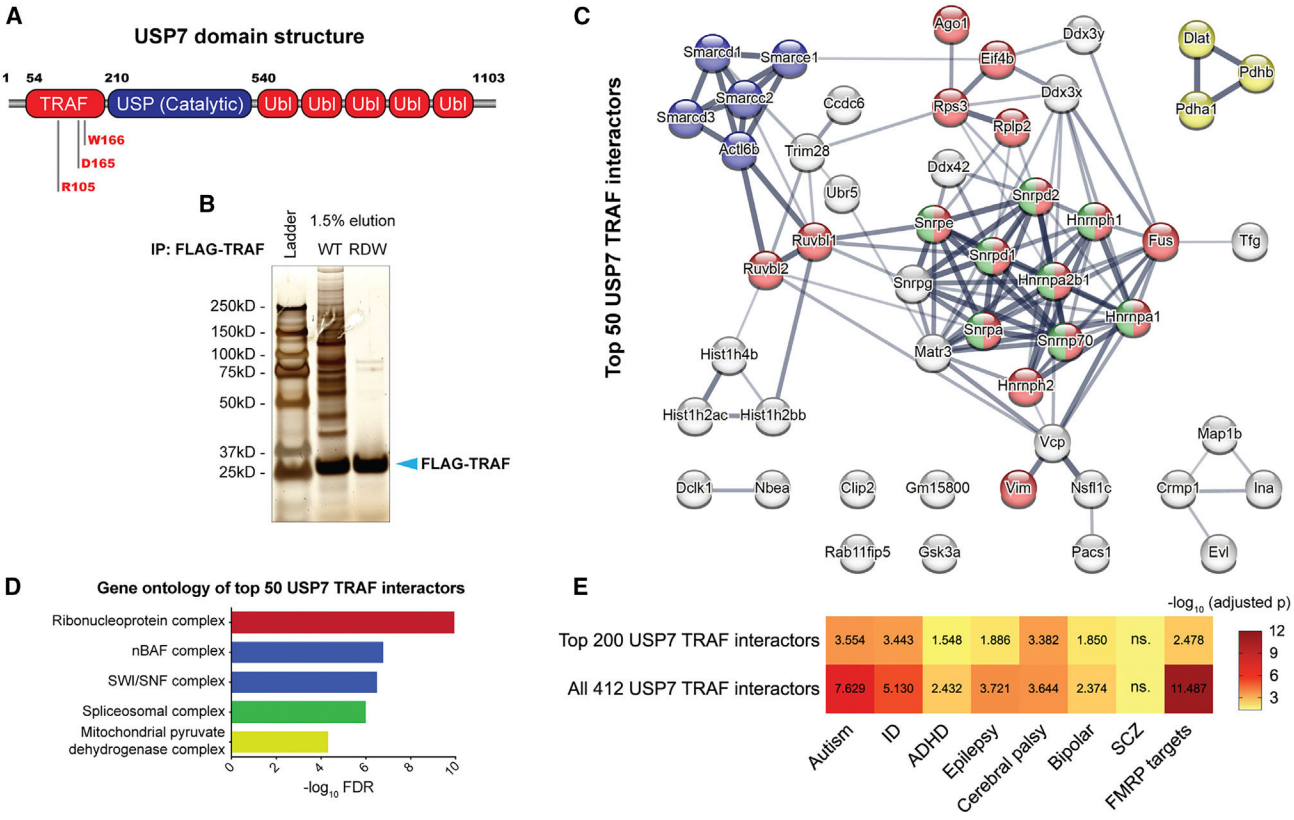

Figure 4. Interactome of the USP7 TRAF domain in cortical neurons

(A) Domain structure of mouse USP7 protein. R105, D165, and W165 are three amino acids necessary for substrate binding.[18,23] USP, ubiquitin-specific protease domain; Ubl, ubiquitin-like domain.

(B) Silver staining of the FLAG-immunoprecipitated USP7 TRAF domain (arrowhead) with and without RDW mutations (R105A+D165A+W166A).

(C) Protein-protein association map of the top 50 USP7 TRAF interactors (full STRING network, confidence > 0.4). Proteins in complexes are colored according to (D).

(D) GO analysis (cellular component) of the top 50 USP7 TRAF interactors. nBAF complex, neuronal SWI/SNF (BAF) complex.

(E) Heatmap showing adjusted p values for enrichment of the USP7 TRAF interactors in disease genes. ID, intellectual disability; ADHD, attention deficit hyperactivity disorder; SCZ, schizophrenia; Ns, not significant. The *p* values were calculated by one-sided hypergeometric test with Benjamini-Hochberg correction.

See also Figure S5.

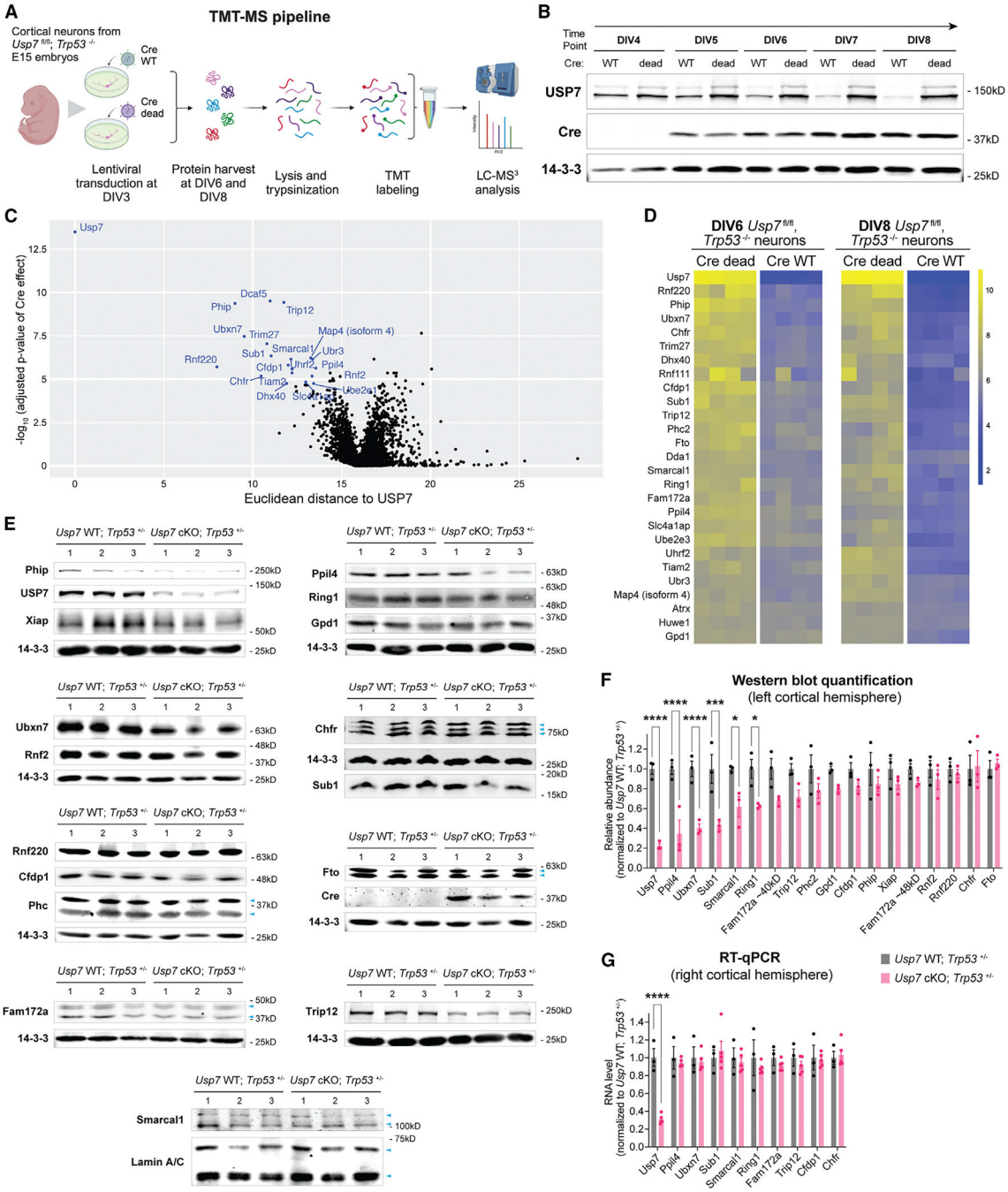

Figure 5. Acute USP7 loss transforms the proteome of cortical neurons and depletes candidate substrate at the protein level

(A) Flowchart to characterize dynamics of the neuronal proteome in response to acute *Usp7* knockout with 16-plex TMT-MS.

(B) Immunoblot of USP7 depletion and Cre expression in primary cortical neurons over time. 14–3-3 is the loading control.

(C) Volcano plot showing candidate substrates of USP7. Euclidean distances to USP7 were calculated in the space of TMT protein abundance. The *p* values were calculated by two-way ANOVA for Cre effect with Benjamini–Hochberg correction.

(D) Heatmap of TMT protein abundance of USP7 and its candidate substrates.
(E and F) Immunoblot images (E) and densitometric quantification (F) of candidate substrates in the cerebral cortex of *Usp7* cKO; $Trp53^{+/-}$ (n = 3) mice vs. *Usp7* WT; $Trp53^{+/-}$ ($n = 3$) mice at P0. 14–3-3 and lamin A/C are loading controls. Arrowheads indicate multiple specific bands of a single candidate substrate. $*p < 0.05$, $***p < 0.001$, $****p < 0.0001$ by Šídák multiple-comparisons test.
(G) RT-qPCR of candidate substrates in the cerebral cortex of *Usp7* cKO; $Trp53^{+/-}$ ($n = 5$) mice vs. *Usp7* WT; $Trp53^{+/-}$ ($n = 3$) mice at P0. $****p < 0.0001$ by Šídák multiple-comparisons test.
Data are presented as mean ± SEM. See also Figure S6.

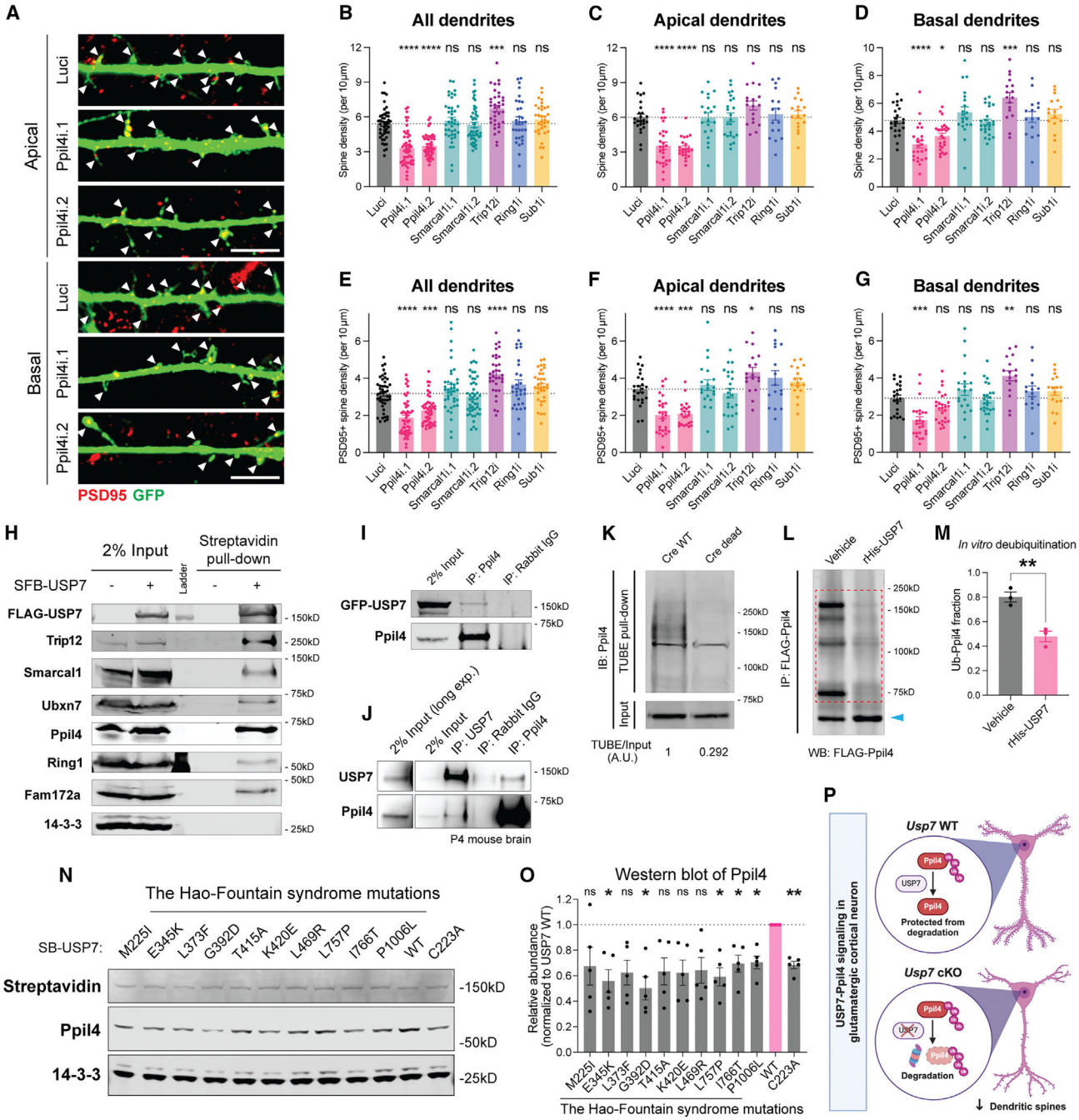

Figure 6. USP7 targets and deubiquitinates Ppil4 to promote dendritic spinogenesis

(A) Representative GFP and PSD95 micrographs of dendritic spines (arrowheads) of DIV18 primary cortical neurons with knockdown of Ppil4 or luciferase (Luci). Micrographs of dendritic spines with knockdown of other candidate substrates are shown in Figure S8. Scale bar, 5 μm.

(B–G) Density of all (B–D) and PSD95+ (E–G) spines on apical, basal, and all dendrites of cortical neurons. *$p < 0.05$, **$p < 0.01$, ***$p < 0.001$, ****$p < 0.0001$ by Dunnett's multiple-comparisons test (compared to Luci).

(H) Streptavidin pull-down of HEK293T lysate with overexpression of streptavidin-binding peptide-FLAG (SFB)-tagged USP7 followed by immunoblot analyses.
(I) IP of endogenous Ppil4 in HEK293T lysates followed by immunoblot analyses.
(J) Reciprocal IP of endogenous USP7 and Ppil4 in mouse brain at age P4, followed by immunoblot analyses. Input lysate with long exposure for clear visualization is shown on the left.
(K) TUBE pull-down of MG132-treated neuronal lysate with USP7 loss driven by lentiviral Cre followed by immunoblotting of Ppil4. Densitometric quantification is shown at the bottom. IB, immunoblot; a.u., arbitrary unit.
(L and M) *In vitro* deubiquitination using FLAG-immunoprecipitated Ppil4 from MG132-treated HEK293T cells (L) and densitometric quantification (M) of high-molecular-weight Ppil4 over all Ppil4 signals with 3 biological replicates. $^{**}p < 0.01$ by 2-tailed unpaired t test.
(N and O) Immunoblot and densitometric quantification ($n = 5$ biological replicates) of endogenous Ppil4 in HEK293T cells expressing patient variants of USP7. USP7 C223A is catalytically dead as a positive control. $^{*}p < 0.05$, $^{**}p < 0.01$ by Dunnett's multiple-comparisons test after repeated-measurement one-way ANOVA.
(P) Schematic of the USP7-Ppil4 signaling pathway regulating dendritic spines.
Data are presented as mean ± SEM. See also Figure S7.

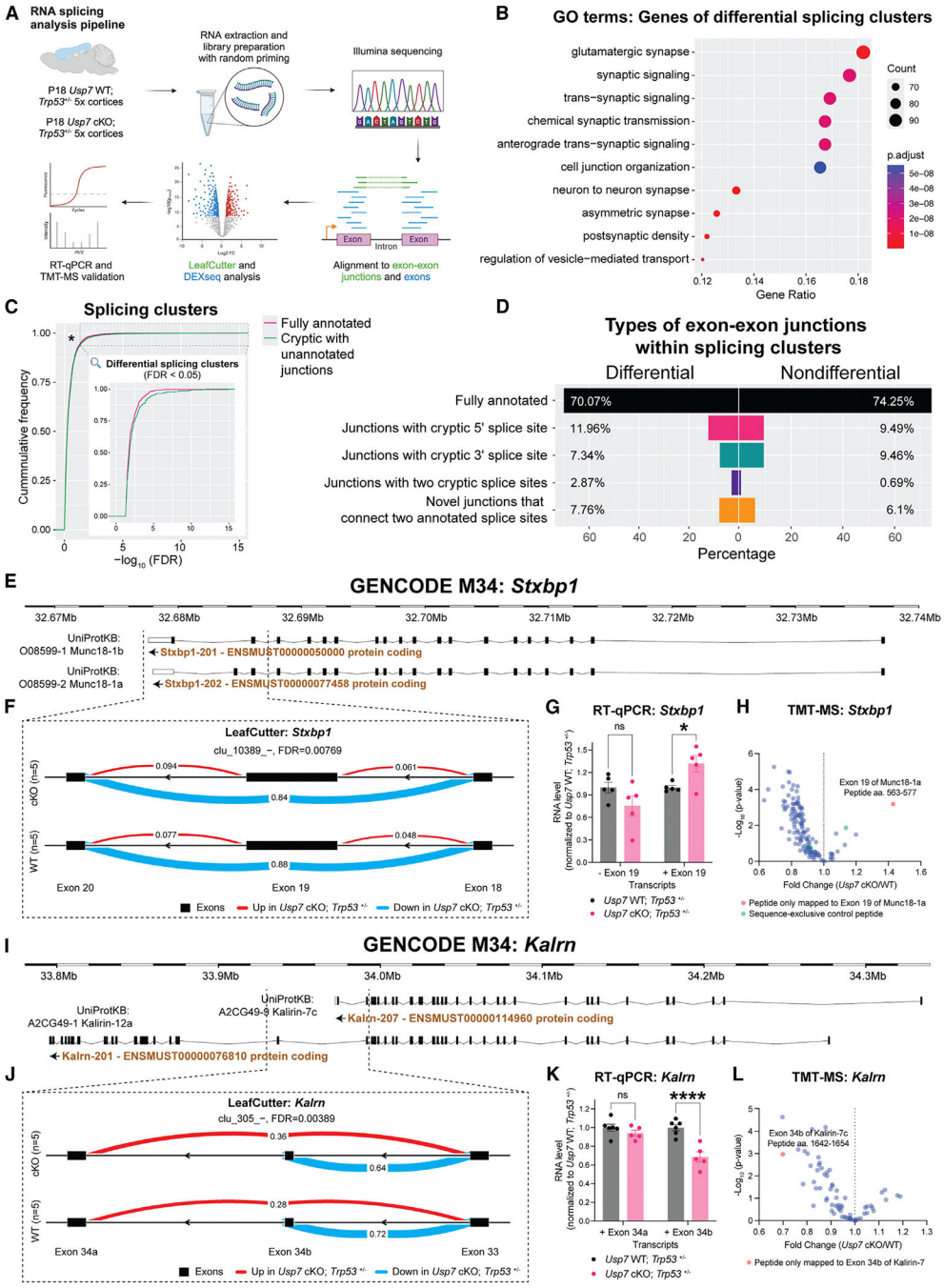

Figure 7. USP7 loss disrupts RNA splicing of synaptic genes in the cerebral cortex

(A) Flowchart to analyze RNA splicing upon USP7 loss.

(B) GO terms enriched from genes of differential splicing clusters in LeafCutter analysis (FDR < 0.05 between *Usp7* WT; *Trp53*$^{+/-}$ and *Usp7* cKO; *Trp53*$^{+/-}$ mice).

(C) Cumulative frequency curves of LeafCutter FDR of fully annotated and cryptic splicing clusters. Cumulative frequency curves for differential splicing clusters are expanded in the inset. *$p < 0.05$ by Kolmogorov-Smirnov test.

(D) Percentage breakdown of exon-exon junction subtypes in differential and nondifferential splicing clusters.
(E) Gene structure of *Stxbp1*.
(F–H) Inclusion of exon 19 of *Stxbp1*, shown by LeafCutter sashimi plot (F), isoform-specific RT-qPCR bar plot (G), and volcano plot of all peptides mapped to *Stxbp1* in TMT-MS (H). *$p < 0.05$ by uncorrected Fisher's least significant difference (LSD) multiple-comparisons test.
(I) Gene structure of *Kalrn*.
(J–L) Usage of exon 34a or exon34b of *Kalrn*, shown by LeafCutter sashimi plot (J), isoform-specific RT-qPCR bar plot (K), and volcano plot of all peptides mapped to *Stxbp1* in TMT-MS (L). ****$p < 0.0001$ by uncorrected Fisher's LSD multiple-comparisons test. Data are presented as mean ± SEM. See also Figures S8 and S9.

KEY RESOURCES TABLE

REAGENT or RESOURCE	SOURCE	IDENTIFIER
Antibodies		
Rabbit anti-USP7 (immunoblotting and immunoprecipitation)	Bethyl labs	Cat# A300-033A, RRID:AB_203276
Rabbit anti-USP7 (Immunofluorescence)	Bethyl labs	Cat# IHC-00018, RRID:AB_2214171
Mouse anti-NeuN	Millipore	Cat# MAB377, RRID:AB_2298767
Rat anti-Ki67 (SolA15)	Thermo Fisher Scientific	Cat# 14-5698-82, RRID: AB_10854564
Rabbit anti-Cleaved caspase-3	Cell signaling	Cat# 9661, RRID:AB_2341188
Chicken anti-GFP (immunoblotting and immunofluorescence)	Abcam	Cat# ab13970, RRID:AB_300798
Rabbit anti-GFP (Immunoprecipitation)	Homemade	N/A
Mouse anti-mCherry (1C51)	Novus Biological	Cat# NBP1-96752, RRID:AB_11034849
Mouse anti-Cre (2D8) (immunofluorescence)	Millipore	Cat# MAB3120, RRID:AB_2085748
Rabbit anti-Cre (immunoblotting)	Millipore	Cat# 69050, RRID:AB_10806983
Mouse anti-Myc (9e10)	Santa Cruz Biotechnology	Cat# sc-40, RRID:AB_627268
Mouse anti-FLAG (M2)	Sigma	Cat# F3165, RRID:AB_259529
Mouse anti-FLAG M2 agarose beads	Sigma	Cat# A2220, RRID:AB_10063035
Rabbit anti-HA (C29F4)	Cell Signaling	Cat# 3724, RRID:AB_1549585
Rabbit anti-Map2	Abcam	Cat# ab32454, RRID:AB_776174
Rabbit anti-Phip	Bethyl labs	Cat# A302-054A, RRID:AB_1604219
Rabbit anti-Xiap	Bioss Antibodies	Cat# bs-1281 R, RRID:AB_10856518
Rabbit anti-Fto	Abclonal	Cat# A1438, RRID:AB_2761247
Rabbit anti-Rnf220	Abclonal	Cat# A15853, RRID:AB_2763280
Rabbit anti-Cfdp1	Bethyl labs	Cat# A305-624A, RRID:AB_2891537
Rabbit anti-Phc2	Abclonal	Cat# A14727, RRID:AB_2761604
Rabbit anti-Ppil4 (immunoprecipitation)	Bethyl labs	Cat# A304-965A, RRID:AB_2621159
Rabbit anti-Ppil4 (immunoblotting)	Sigma	Cat# HPA031600, RRID:AB_10600928
Rabbit anti-Gpd1	Abclonal	Cat# A5715, RRID:AB_2766473
Rabbit anti-Smarcal1	Millipore	Cat# ABE1836, RRID:AB_3662942
Rabbit anti-Ubxn7	Bethyl labs	Cat# A303-865A, RRID:AB_2620216
Rabbit anti-Rnf2	Abclonal	Cat# A5563, RRID:AB_2766343
Rabbit anti-Trip12	Abclonal	Cat# A9958, RRID:AB_2772719
Rabbit anti-Fam172a	Novus Biological	Cat# NBP1-86774, RRID:AB_11036426
Rabbit anti-Sub1/PC4	Cohesion Biosciences	Cat# CQA1533, RRID:AB_3662943
Rabbit anti-Chfr	Abclonal	Cat# A10447, RRID:AB_2757994
Mouse anti-Ruvbl2	Santa Cruz	Cat# sc-374135, RRID:AB_10915735
Mouse anti-Ring1 (8C12F4)	Novus Biological	Cat# NBP2-37370, RRID:AB_3296277
Mouse anti-14-3-3	Santa Cruz Biotechnology	Cat# sc-25276, RRID:AB_626617
Mouse anti-Lamin A/C (4C11)	Cell signaling	Cat# 4777, RRID:AB_10545756
Mouse anti-PSD95 (K28/43)	NeuroMab	Cat# 75-028, RRID:AB_2292909
Normal Rabbit IgG	Cell signaling	Cat# 2729, RRID:AB_1031062
IRDye 800CW Donkey anti-Rabbit IgG antibody	LI-COR	Cat# 925-32213, RRID:AB_2715510

REAGENT or RESOURCE	SOURCE	IDENTIFIER
IRDye 800CW Donkey anti-Chicken IgG antibody	LI-COR	Cat# 926-32218, RRID:AB_1850023
IRDye 680CW Donkey anti-Mouse IgG antibody	LI-COR	Cat# 926-32222, RRID:AB_621844
Goat anti-Mouse IgG (H + L) Cross-Adsorbed Secondary Antibody, Alexa Fluor 488	Thermo Fisher Scientific	Cat# A-11001, RRID:AB_2534069
Goat anti-Rat IgG (H + L) Cross-Adsorbed Secondary Antibody, Alexa Fluor 488	Thermo Fisher Scientific	Cat# A-11006, RRID:AB_2534074
Goat anti-Rabbit Ig (H + L) Cross-Adsorbed Secondary Antibody, Alexa Fluor 488	Thermo Fisher Scientific	Cat# A-11008, RRID:AB_143165
Goat anti-Chicken IgY (H + L) Secondary Antibody, Alexa Fluor 488	Thermo Fisher Scientific	Cat# A-11039, RRID:AB_2534096
Goat anti-Rabbit IgG (H + L) Cross-Adsorbed Secondary Antibody, Alexa Fluor 568	Thermo Fisher Scientific	Cat# A-11011, RRID:AB_143157
Goat anti-Mouse IgG (H + L) Cross-Adsorbed Secondary Antibody, Alexa Fluor 568	Thermo Fisher Scientific	Cat# A-11004, RRID:AB_2534072
Bacterial and virus strains		
Lentivirus	This study	N/A
AAV PHP.eB	Hope Center Viral Vectors Core at Washington University	N/A
Chemicals, peptides, and recombinant proteins		
MG132	Sigma	Cat# 474790
Bradford reagent	Bio-Rad	Cat# 5000006
RIPA buffer	Cell Signaling	Cat# 9806
Protease inhibitor cocktail	Sigma	Cat# P8340
Phosphatase inhibitor mini-tablet	Thermo Fisher Scientific	Cat# A32957
Hoechst 33258 solution	Sigma	Cat# 94403
3x FLAG peptide	APExBio	Cat# A6001
Protein A Sepharose beads	GE Healthcare	Cat# GE17-5280-01
Veriblot for IP detection reagent (HRP)	Abcam	Cat# ab131366
Dynabeads™ MyOne™ Streptavidin T1	Invitrogen	Cat# 65601
TUBE 2 magnetic beads	LifeSensors	Cat# UM-0402M
Recombinant His-USP7	R&D Systems	Cat# E-519
IRDye 800CW Streptavidin	LI-COR	Cat# 926-32230
EPPS	Alfa Aesar	Cat# AAJ61476AE
Pierce Trypsin Protease, MS Grade	Thermo-Fisher Scientific	Cat# 90058
Lys-C, Mass Spectrometry Grade	Wako Chemicals	Barcode# 4987481427648
Deposited data		
IP mass spectrometry data	ProteomeXchange	PXD043225
TMT proteomics data	ProteomeXchange	PXD043848
TMT proteomics data	ProteomeXchange	PXD043849
RNA-seq data	GEO	GSE280944
Experimental models: Cell lines		

REAGENT or RESOURCE	SOURCE	IDENTIFIER
HEK293T/HEK293LE	Clontech	Cat# 632180
Experimental models: Organisms/strains		
NEX-Cre mice on C57BL/6J	Goebbels et al.[19]	N/A
Usp7$^{fl/fl}$ mice on hybrid C57BL/6J and 129Sv	Kon et al.[15]	N/A
Usp7$^{fl/fl}$ mice on C57BL/6J	This study	N/A
Trp53 KO mice on C57BL/6J	The Jackson Laboratory	Cat# 002101
Wild-type outbred mice on CD1	Charles River	Cat# 022
Wild-type inbred mice on C57BL/6J	The Jackson Laboratory	Cat# 000664
Oligonucleotides		
See Table S2	N/A	N/A
Recombinant DNA		
pCMV-myc3-Mdm2	Addgene, Zhang et al.[59]	Cat# 20935, RRID:Addgene_20935
pAAV-hSyn1-EGFP-P2A-EGFPf-WPRE-HGHpA	Addgene, Zhang et al.[60]	Cat# 74513, RRID:Addgene_74513
pMH-SFB-USP7	Addgene, An et al.[61]	Cat# 99393, RRID:Addgene_99393
pEGFP-USP7	Anckar et al.[6]	N/A
pEGFP-USP7 1-209	This study	N/A
pEGFP-USP7 55-209 (TRAF)	This study	N/A
pMH-SB-USP7	This study	N/A
pMH-SB-USP7 M225I	This study	N/A
pMH-SB-USP7 E345K	This study	N/A
pMH-SB-USP7 L373F	This study	N/A
pMH-SB-USP7 G392D	This study	N/A
pMH-SB-USP7 T415A	This study	N/A
pMH-SB-USP7 K420E	This study	N/A
pMH-SB-USP7 L469R	This study	N/A
pMH-SB-USP7 L757P	This study	N/A
pMH-SB-USP7 I766T	This study	N/A
pMH-SB-USP7 P1006L	This study	N/A
pMH-SB-USP7 C223A	This study	N/A
pHAGE-hSyn-FLAG-USP7 55-209 (TRAF)	This study	N/A
FCIV.1-Cre-IRES-mCherry	This study	N/A
FCIV.1-Cre Y331F-IRES-mCherry (Cre dead)	This study	N/A
pcDNA3.1-FLAG-Ppil4	This study	N/A
Software and algorithms		
ImageJ-Fiji	National Institutes of Health, USA	https://github.com/fiji/fiji
Zen	Zeiss	N/A
Imaris	Oxford Instruments	N/A

REAGENT or RESOURCE	SOURCE	IDENTIFIER
Image Studio	Li-Cor	N/A
Proteomics software pipeline #1	SEQUEST	http://fields.scripps.edu/yates/wp/?page_id=17
Proteomics software pipeline #2	Comet	https://uwpr.github.io/Comet/
GSEA (v4.3.2)	UC San Diego, Broad Institute	https://www.gsea-msigdb.org/gsea/index.jsp
Cytoscape (v3.9.1)	National Institute of General Medical Sciences	https://cytoscape.org/
ITK-SNAP (v3.8)	NYU, Tanden School of Engineering	www.itksnap.org
Prism (v.9)	GraphPad	N/A
SPSS (v.26)	IBM	N/A
R	The R project	N/A